Monthly Notices
of the
ROYAL ASTRONOMICAL SOCIETY

MNRAS **474,** 5076–5104 (2018)
Advance Access publication 2017 November 23

doi:10.1093/mnras/stx3016

The KMOS Redshift One Spectroscopic Survey (KROSS): the origin of disc turbulence in $z \approx 1$ star-forming galaxies

H. L. Johnson,[1★] C. M. Harrison,[1,2] A. M. Swinbank,[1,3] A. L. Tiley,[1,4] J. P. Stott,[4,5] R. G. Bower,[1,3] Ian Smail,[1,3] A. J. Bunker,[4,6] D. Sobral,[5,7] O. J. Turner,[2,8] P. Best,[8] M. Bureau,[4] M. Cirasuolo,[2] M. J. Jarvis,[4,9] G. Magdis,[10,11] R. M. Sharples,[1,12] J. Bland-Hawthorn,[13] B. Catinella,[14] L. Cortese,[14] S. M. Croom,[13,15] C. Federrath,[16] K. Glazebrook,[17] S. M. Sweet,[17] J. J. Bryant,[13,15,18] M. Goodwin,[18] I. S. Konstantopoulos,[18] J. S. Lawrence,[18] A. M. Medling,[16] M. S. Owers[18,19] and S. Richards[20]

Affiliations are listed at the end of the paper

Accepted 2017 November 21. Received 2017 November 21; in original form 2017 July 5

ABSTRACT

We analyse the velocity dispersion properties of 472 $z \sim 0.9$ star-forming galaxies observed as part of the KMOS Redshift One Spectroscopic Survey (KROSS). The majority of this sample is rotationally dominated (83 ± 5 per cent with $v_C/\sigma_0 > 1$) but also dynamically hot and highly turbulent. After correcting for beam smearing effects, the median intrinsic velocity dispersion for the final sample is $\sigma_0 = 43.2 \pm 0.8\,\mathrm{km\,s^{-1}}$ with a rotational velocity to dispersion ratio of $v_C/\sigma_0 = 2.6 \pm 0.1$. To explore the relationship between velocity dispersion, stellar mass, star formation rate, and redshift, we combine KROSS with data from the SAMI survey ($z \sim 0.05$) and an intermediate redshift MUSE sample ($z \sim 0.5$). Whilst there is, at most, a weak trend between velocity dispersion and stellar mass, at fixed mass there is a strong increase with redshift. At all redshifts, galaxies appear to follow the same weak trend of increasing velocity dispersion with star formation rate. Our results are consistent with an evolution of galaxy dynamics driven by discs that are more gas rich, and increasingly gravitationally unstable, as a function of increasing redshift. Finally, we test two analytic models that predict turbulence is driven by either gravitational instabilities or stellar feedback. Both provide an adequate description of the data, and further observations are required to rule out either model.

Key words: galaxies: evolution – galaxies: high-redshift – galaxies: kinematics and dynamics – infrared: galaxies.

1 INTRODUCTION

The past decade has seen significant advancements in our understanding of the high-redshift Universe. The cosmic star formation rate (SFR) density peaks in the redshift range $z \sim 1$–3 (e.g. Lilly et al. 1996; Karim et al. 2011; Burgarella et al. 2013; Sobral et al. 2013a), and so establishing the properties of galaxies at this epoch is key to constraining models of galaxy formation and evolution. It is at this crucial time that today's massive galaxies formed the bulk of their stars. The increased activity is thought to be driven (at least in part) by high molecular gas fractions (e.g. Daddi et al. 2010; Tacconi et al. 2010, 2013; Saintonge et al. 2013; Genzel et al. 2015), which may naturally explain the clumpy and irregular morphologies prevalent in *Hubble Space Telescope* (*HST*) images (e.g. Livermore et al. 2012, 2015).

The introduction of integral field spectroscopy (e.g. see Glazebrook 2013 for review) has been pivotal in allowing us to resolve the internal complexities of distant galaxies. Each spatial pixel of an integral field unit (IFU) is associated with a spectrum such that galaxy kinematics, star formation, and metallicity can be mapped. Early studies often involved the in-depth analysis of small samples, since observations were time-consuming (e.g. Förster Schreiber et al. 2006; Law et al. 2009; Lemoine-Busserolle et al. 2010;

★ E-mail: helenjn@blueyonder.co.uk

© 2017 The Author(s)
Published by Oxford University Press on behalf of the Royal Astronomical Society

Downloaded from https://academic.oup.com/mnras/article-abstract/474/4/5076/4655192 by University of Queensland Library user on 07 February 2020

Swinbank et al. 2012a). However, second-generation instruments such as the *K*-band Multi-Object Spectrograph (KMOS; Sharples et al. 2004, 2013) now allow for the simultaneous observation of multiple targets and as such we can construct large and well-selected samples in reasonable exposure times (e.g. Wisnioski et al. 2015; Stott et al. 2016).

A surprising discovery has been that whilst high-redshift samples are kinematically diverse, with a higher incidence of mergers than observed locally (e.g. Molina et al. 2017), many galaxies appear to be rotationally supported (e.g. Förster Schreiber et al. 2009; Epinat et al. 2012; Wisnioski et al. 2015; Stott et al. 2016; Harrison et al. 2017, although see also Di Teodoro, Fraternali & Miller 2016). Often despite morphological irregularity, the dynamical maps of these galaxies reveal a smooth, continuous velocity gradient. Clumps visible in broad-band imaging appear to be giant star-forming complexes (e.g. Genzel et al. 2011; Livermore et al. 2012; Swinbank et al. 2012b; Wisnioski et al. 2012) that are embedded within the disc and share the same underlying dynamics.

The existence of settled discs supports the emerging consensus that a galaxy's star formation history is not dominated by mergers but by an ongoing accretion of gas from the cosmic web (Dekel, Sari & Ceverino 2009; Ceverino, Dekel & Bournaud 2010). Observations of a tight relation between stellar mass and SFR (the so-called galaxy main sequence; Noeske et al. 2007; Elbaz et al. 2011; Karim et al. 2011) are considered further evidence of this. A gradual decrease in the available gas supply would explain the evolution of this trend as a function of redshift, whereas stochastic, merger-driven bursts would introduce significantly more scatter.

Kinematic surveys have revealed that whilst typical rotation velocities of high-redshift discs are similar to those seen locally, intrinsic velocity dispersions are much higher (e.g. Genzel et al. 2008; Lehnert et al. 2009; Gnerucci et al. 2011; Epinat et al. 2012; Newman et al. 2013; Wisnioski et al. 2015; Di Teodoro et al. 2016; Turner et al. 2017a). These dispersions are supersonic and most likely represent turbulence within the interstellar medium (ISM). Measurements are consistently large, both for natural seeing observations and for those that exploit adaptive optics (e.g. Law et al. 2009; Wisnioski et al. 2011) or gravitational lensing (e.g. Stark et al. 2008; Jones et al. 2010). Whilst most high-redshift studies use emission lines such as Hα or [O II] to trace the ionized gas dynamics of galaxies, observations of spatially resolved CO emission have been made (e.g. Tacconi et al. 2010, 2013; Swinbank et al. 2011; Genzel et al. 2013). These studies suggest that the molecular gas is also turbulent – it is the entire disc that is dynamically hot, and not just 'flotsam' on the surface that has been stirred up by star formation (see also Bassett et al. 2014).

Since turbulence in the ISM decays on time-scales comparable to the disc crossing time, a source of energy is required to maintain the observed high-velocity dispersions (e.g. Mac Low et al. 1998; Stone, Ostriker & Gammie 1998). Several potential mechanisms have been suggested, including star formation feedback (e.g. Lehnert et al. 2009; Le Tiran et al. 2011; Green et al. 2010; Lehnert et al. 2013), accretion via cosmological cold flows (Klessen & Hennebelle 2010), gravitational disc instabilities (e.g. Bournaud et al. 2010, 2014; Ceverino et al. 2010; Goldbaum, Krumholz & Forbes 2015), interactions between star-forming clumps (Dekel et al. 2009; Aumer et al. 2010), or some combination thereof. However, there have been few observational tests of these theories.

Recent advancements in instrumentation such as multi-IFU systems [e.g. KMOS, Sydney/AAO Multi-object Integral-field spectrograph (SAMI); Croom et al. 2012; Sharples et al. 2013] and panoramic IFUs [e.g. Multi-Unit Spectroscopic Explorer (MUSE); Bacon et al. 2010] allow for large, un-biased samples to be subdivided into bins of redshift, SFR, stellar mass, and morphology. In this work, we investigate the velocity dispersion properties of high-redshift galaxies using data from the KMOS Redshift One Spectroscopic Survey (KROSS; Stott et al. 2016). This mass-selected parent sample targeted with KMOS consists of ∼800 Hα-detected, typical star-forming galaxies at $z \sim 1$. Of these galaxies observed with KMOS, 586 are detected in Hα, and these are the sample analysed in this paper. We further supplement these observations with data from SAMI ($z \sim 0.05$) and an intermediate redshift MUSE sample ($z \sim 0.5$).

We organize the paper as follows. In Section 2, we describe the KROSS survey, sample selection, and observations. In Section 3, we outline our analysis, the measurement of kinematic quantities, and corrections applied for beam smearing. In Section 4, we present our results. We discuss how velocity dispersion relates to SFR and stellar mass, and explore how galaxy dynamics evolve as a function of redshift. In Section 5, we investigate which physical processes may drive turbulence in the ISM, using KROSS to test the predictions of analytic models. Finally, in Section 6, we summarize our main conclusions. In this work, we adopt a $H_0 = 70\,\mathrm{km\,s^{-1}\,Mpc^{-1}}$, $\Omega_\mathrm{M} = 0.3$, and $\Omega_\Lambda = 0.7$ cosmology. We assume a Chabrier IMF (Chabrier 2003) and quote all magnitudes as AB. Throughout, the errors associated with median values are estimated from a bootstrap re-sampling of the data.

2 SURVEY PROPERTIES, SAMPLE SELECTION, AND DATA REDUCTION

KROSS is an ESO Guaranteed Time survey (PI: R. Sharples) designed to study the spatially resolved dynamics of typical $z \sim 1$ star-forming galaxies using KMOS. With 24 individual near-infrared IFUs, the high multiplexing capability of KMOS has allowed us to efficiently construct a statistically significant sample at this epoch. The programme is now complete, with a total of 795 galaxies observed. Full details of the sample selection, observations, and data reduction can be found in Stott et al. (2016) and Harrison et al. (2017); however, in the following subsections, we briefly summarize the key aspects.

2.1 Sample selection

The main aim of KROSS is to study the ionized gas kinematics of a large and representative sample of star-forming galaxies at $z \sim 1$. We use KMOS to target the Hα emission line that combined with the adjacent [N II] doublet allows us to trace star formation, dynamics, and chemical abundance gradients. Targets were selected such that Hα is redshifted into the *YJ* band and are located in the following extragalactic fields: (1) Cosmological Evolution Survey (COSMOS); (2) Extended *Chandra* Deep Field South (ECDFS); (3) SA22, and (4) UKIDSS Ultra-Deep Survey (UDS).

In addition to these redshift criteria, we prioritized galaxies with an observed *K*-band magnitude of $K_\mathrm{AB} < 22.5$, which translates to a stellar mass of $\log(M_\star/\mathrm{M}_\odot) \gtrsim 9.5$ at this redshift (see Section 2.2), and with colours of $r - z < 1.5$. For completeness, redder galaxies (more passive or potentially more dust obscured) were also included but were assigned a lower priority for observation. Our sample therefore favours star-forming and unobscured galaxies that may have strong line emission.

From the original KROSS parent sample of 795 galaxies that were targeted with KMOS, we follow Harrison et al. (2017) and

Downloaded from https://academic.oup.com/mnras/article-abstract/474/4/5076/4655192 by University of Queensland Library user on 07 February 2020

first remove 52 galaxies that have unreliable photometry, or suffered from KMOS pointing errors. The remaining sample consists of 743 galaxies between $z = 0.6$ and 1.0, with a median redshift of $z = 0.85^{+0.11}_{-0.04}$. Of these, 586 are detected in Hα, with a total signal-to-noise ratio (S/N) in the one-dimensional spectrum [integrated over the full width at half-maximum (FWHM) of the Hα emission line] of S/N > 5. These 586 galaxies are used for dynamical analysis described in this paper.

2.2 Stellar masses

Since many our targets lie in deep extragalactic survey fields, a wealth of archival photometry data (from X-ray to radio) exists. Wherever possible, we use imaging from the *U*-band through IRAC 8.0 μm to derive the best-fitting SEDs and absolute magnitudes. Briefly, we applied the SED-fitting code HYPERZ (Bolzonella, Miralles & Pelló 2000) to fit *U* band through 4.5 μm photometry using spectral templates derived from the Bruzual & Charlot (2003) evolutionary code. The model SEDs are characterized by star formation histories that are parametrized by age and reddening. We use the solar metallicity templates and consider seven star formation histories (Burst, Constant, and six exponentially declining models with $\tau = 1$, 2, 3, 5, 15, and 30 Gyr). We allow stellar reddening (A_V) of 0–5 mag in steps of 0.1 and follow the Calzetti et al. (2000) attenuation law.

Although individual estimates of stellar mass can be made from the best-fitting star formation histories, for consistency with Harrison et al. (2017), and for the sake of reproducibility and homogeneity within our analysis, we apply a single mass-to-light ratio to ensure consistency across the four target fields. This also allows homogeneity with the lower-redshift MUSE comparison sample, where there is often no long wavelength IRAC data (which is needed to break some of the degeneracies in the SED fitting between young/dusty versus old stellar populations). To derive stellar masses, we convert rest-frame *H*-band absolute magnitudes using the median mass-to-light ratio returned by HYPERZ ($\Upsilon_H = 0.2$), as $M_\star = \Upsilon_H \times 10^{-0.4\times(M_H - 4.71)}$, resulting in a median stellar mass of $\log(M_\star/\mathrm{M}_\odot) = 10.0 \pm 0.4$.

We note that adopting a single mass-to-light ratio or dust attenuation for the SFRs (see Section 2.3) may over- or underestimate the stellar masses. However, over the range of $M_\star = 5 \times 10^9$ –5×10^{11} $\mathrm{M}_\odot$ the stellar masses as measured from the star formation histories (accounting for mass loss) and estimates made by adopting a single mass-to-light ratio typically agree to within 30 per cent. Moreover, we do not identify a strong trend in dust attenuation, with A_V varying by less than 0.3 mag over this same stellar mass range.

2.3 Star formation rates

We find a median Hα luminosity for the KROSS sample of $\log(L_{\mathrm{H}\alpha}/\mathrm{erg\,s^{-1}}) = 41.5 \pm 0.3$, which equates to $\sim 0.6 \times L^\star_{\mathrm{H}\alpha}$ at $z \sim 1$ (Sobral et al. 2015). To convert to SFRs, we adopt a simple approach and apply the Kennicutt (1998) calibration (using a Chabrier IMF; Chabrier 2003), assuming a dust attenuation of $A_{\mathrm{H}\alpha} = 1.73$ (the median for the sample as returned by HYPERZ, converted from stellar to gas extinction using the relation from Wuyts et al. 2013). From this method, we derive a median SFR of $7.0 \pm 0.3\,\mathrm{M}_\odot\,\mathrm{yr}^{-1}$ (see also Harrison et al. 2017).

In Fig. 1, we plot Hα luminosity versus estimated stellar mass for the 586 galaxies detected in Hα. We overlay the star-forming 'main sequence' (as described by Speagle et al. 2014) at the median redshift of KROSS and find the properties of our sample to be consistent with this trend. Approximately, 95 per cent of galaxies have SFRs within a factor of 5 of the median for their mass. We therefore conclude that our sample appears to be representative of typical star-forming galaxies at this redshift.

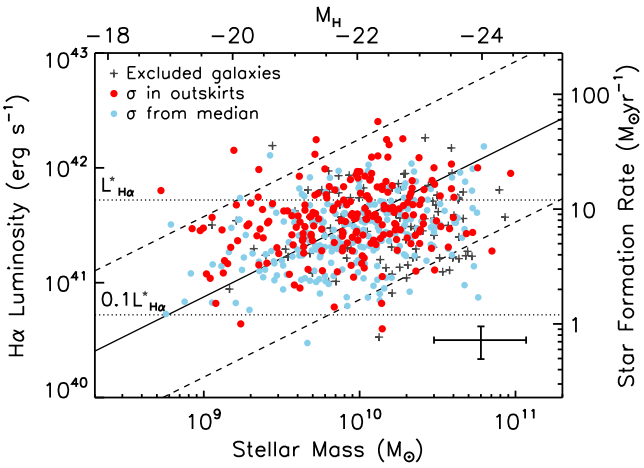

Figure 1. Observed Hα luminosity against stellar mass (scaled from M_H, top axis, assuming a constant mass-to-light ratio) for all 586 Hα-detected KROSS galaxies. Targets cut from the final kinematic sample (potential AGN or mergers, unresolved or low data quality sources; see Section 3.7) are marked by crosses. We differentiate between galaxies for which the dispersion is measured in the outskirts of the disc, and those where it comes from the median of all available pixels (see Section 3.5). We find a median SFR of $7\,\mathrm{M}_\odot\,\mathrm{yr}^{-1}$ and a median stellar mass of $10^{10}\,\mathrm{M}_\odot$, in line with the star-forming 'main sequence' at $z = 0.85$ (Speagle et al. 2014; solid line, with dashed lines a factor of 5 above or below). Dotted lines show $0.1\times$ and $1 \times L_{\mathrm{H}\alpha}$ at this redshift (Sobral et al. 2015). A typical systematic error is shown in the bottom right.

2.4 Observations and data reduction

Full details of the observations and data reduction can be found in Stott et al. (2016); however, the following is a brief summary. Observations for KROSS were taken using KMOS, a near-infrared integral field spectrograph on ESO/VLT. The instrument consists of 24 individual IFUs deployable within a 7.2 arcmin diameter patrol field. Each covers a 2.8×2.8 arcsec field of view with a uniform spatial sampling of 0.2 arcsec. All targets were observed with the *YJ*-band filter that covers a wavelength range of 1.03–1.34 μm, thus allowing us to measure the rest-frame optical properties of our sample. The spectral resolution in this band ranges between $R \sim 3000$ and 4000.

Data were taken primarily between 2013 October and 2015 October using guaranteed time, but was supplemented with some science verification observations (Sobral et al. 2013b; Stott et al. 2014). Median seeing in the *J* band was 0.7 arcsec (which corresponds to a physical scale of 5.4 kpc at the median redshift of our survey), with 92 per cent of observations made during conditions of <1 arcsec, and throughout the analysis, we account for the seeing conditions of individual observations. In Appendix B, we present a detailed investigation into the impact of the seeing on our kinematic measurements (so-called beam smearing). Observations were made in an ABAABAAB nod-to-sky sequence, where A represents time on target and B time on sky. Total on-source integration time was an average of 9 ks per galaxy.

Downloaded from https://academic.oup.com/mnras/article-abstract/474/4/5076/4655192 by University of Queensland Library user on 07 February 2020

Initial data reduction was performed using the standard ESOREX/SPARK pipeline, which dark subtracts, flat-fields and wavelength calibrates individual science frames and applies an additional illumination calibration. Each AB pair was reduced individually, with the temporally closest sky subtracted from each object frame. Further sky subtraction was then performed using residual sky spectra extracted from a series of dedicated sky IFUs (one for each of the three KMOS detectors). Finally, we combined all observations of the same galaxy using a 3σ clipped average and re-sampled on to a pixel scale of 0.1 arcsec. This forms the final data cube that we used to extract Hα and continuum images, and velocity and line of sight velocity dispersion maps discussed in the following sections.

3 ANALYSIS

In this work, we explore the velocity dispersion properties of the KROSS sample, investigating which processes may drive the high levels of disc turbulence typically observed in galaxies at this redshift. We first require measurements of galaxy size, inclination, position angle, rotation velocity, and velocity dispersion. Harrison et al. (2017) discussed how high-resolution broad-band imaging can be combined with KMOS data in order to make robust measurements of kinematic and morphological properties. In the following section, we summarize this analysis. A catalogue of raw and derived properties for all 586 Hα detected targets is available online (see Appendix A). With the release of this paper, this has been updated to include measurements and derived quantities relating to the velocity dispersion, as also provided in Table A1. We also discuss our method for mitigating the effects of beam smearing, with a full, comprehensive analysis presented in Appendix B.

3.1 Broad-band imaging

We used the highest quality broad-band imaging available to measure the half-light radius ($R_{1/2}$), inclination (θ), and position angle (PA_{im}) of each galaxy. For 46 per cent of our sample, there is archival *HST* imaging. All of our targets in ECDFS and COSMOS, and a subset of those in UDS, have been observed with *HST* in the *H*, *I*, or z' band. For all other targets, we use *K*-band ground-based imaging taken with the United Kingdom Infrared Telescope as part of the UKIDSS survey (Lawrence et al. 2007). These images have a typical point spread function (PSF) of FWHM = 0.65 arcsec in UDS and 0.85 arcsec in SA22.

In Harrison et al. (2017), we discuss the implications of using imaging of different rest-frame wavelengths and spatial resolutions, and perform a series of tests to determine any systematics introduced. A small (∼10 per cent) correction is required such that the galaxy sizes measured at different wavelengths are consistent. We also assign greater uncertainties to position angles and inclinations derived from ground-based images to account for the additional scatter introduced to these measurements.

3.2 Sizes, inclinations, and position angles

We first fit each image as a two-dimensional Gaussian profile in order to determine a morphological position angle and best-fitting axis ratio (b/a). We deconvolve for the PSF of the image and convert this axis ratio to an inclination angle as

$$\cos^2\theta_{\rm im} = \frac{(b/a)^2 - q_0^2}{1 - q_0^2}, \quad (1)$$

where q_0 is the intrinsic axial ratio of an edge-on galaxy. This parameter could have a wide range of values (≈0.1–0.65; see Law et al. 2012); however, we adopt the ratio for a thick disc, $q_0 = 0.2$. Adjusting q_0 would not have a significant impact on our results. For 7 per cent of galaxies, we are unable to estimate $\theta_{\rm im}$ due to poor resolution imaging. We therefore assume the median axis ratio of the *HST* observed sources and assign these a 'quality 2' flag (see Section 3.7).

To estimate the half-light radius, we measure the flux of each broad-band image within a series of increasingly large elliptical apertures. For each ellipse, we use the continuum centre, and the position angle and axis ratio derived above. We define $R_{1/2}$ as the radius of the ellipse that contains half the total flux, deconvolved for the PSF of the image.

For 14 per cent of the sample, we are unable to measure the half-light radius from the image, but instead infer an estimate using the turnover radius of the rotation curve ($R_{\rm d}$; see Section 3.4). We calibrate these radii using sources for which both $R_{1/2}$ and $R_{\rm d}$ can be measured, and again assign a 'quality 2' flag. For an additional 6 per cent of sources, neither of these methods were suitable and we therefore place a conservative upper-limit on $R_{1/2}$ of $1.8 \times \sigma_{\rm PSF}$. We assign these a 'quality 3' flag. Quality 3 sources are not included in the results and discussion in Sections 4 and 5 (see also Section 3.7).

3.3 Emission-line fitting

A detailed description of how we extract two-dimensional maps of Hα flux, velocity, and velocity dispersion from the IFU data can be found in Stott et al. (2016); however, we include a brief summary here. In each spatial pixel, we fit the Hα and [N II] $\lambda\lambda$6548, 6583 emission lines via a χ^2 minimization procedure, weighting against the positions of bright OH skylines (Rousselot et al. 2000). Each emission line is modelled as a single Gaussian component within a linear local continuum. We fit the Hα and [N II] emission simultaneously, allowing the centroid, intensity, and width of the Gaussian profile to vary. The FWHM of the lines are coupled, wavelength offsets fixed, and the flux ratio of the [N II] doublet fixed to be 3.06 (Osterbrock & Ferland 2006). During the fitting, we convolve the line profile with the instrumental dispersion, as measured from the widths of nearby skylines. As such, our dispersion measurements are corrected for the instrumental resolution.

If the detection in a given pixel does not exceed an S/N > 5, then we bin the data into successively larger regions, stopping either when this criterion is met or an area of 0.7×0.7 arcsec (the typical seeing of our observations) is reached. Using this method, 552 (94 per cent) of the Hα-detected sample are spatially resolved. We classify all unresolved sources as having a 'quality 4' flag and these are not included in the results and discussion presented in Section 4 and 5 (see also Section 3.7). In Fig. 2, we show example Hα intensity, velocity, and velocity dispersion maps for eight KROSS galaxies.

3.4 Rotation velocities

In order to measure a rotation velocity, we must first establish the position of the major kinematic axis ($PA_{\rm vel}$). We rotate the Hα velocity field around the continuum centre in 1 deg increments and extract a velocity profile each time. We find the profile with the largest velocity gradient and identify this position angle as $PA_{\rm vel}$. To extract a rotation curve along this axis, we calculate the median velocity at positions along a 0.7 arcsec 'slit' through the continuum centre. Example rotation curves are included in Fig. 2, where the

Downloaded from https://academic.oup.com/mnras/article-abstract/474/4/5076/4655192 by University of Queensland Library user on 07 February 2020

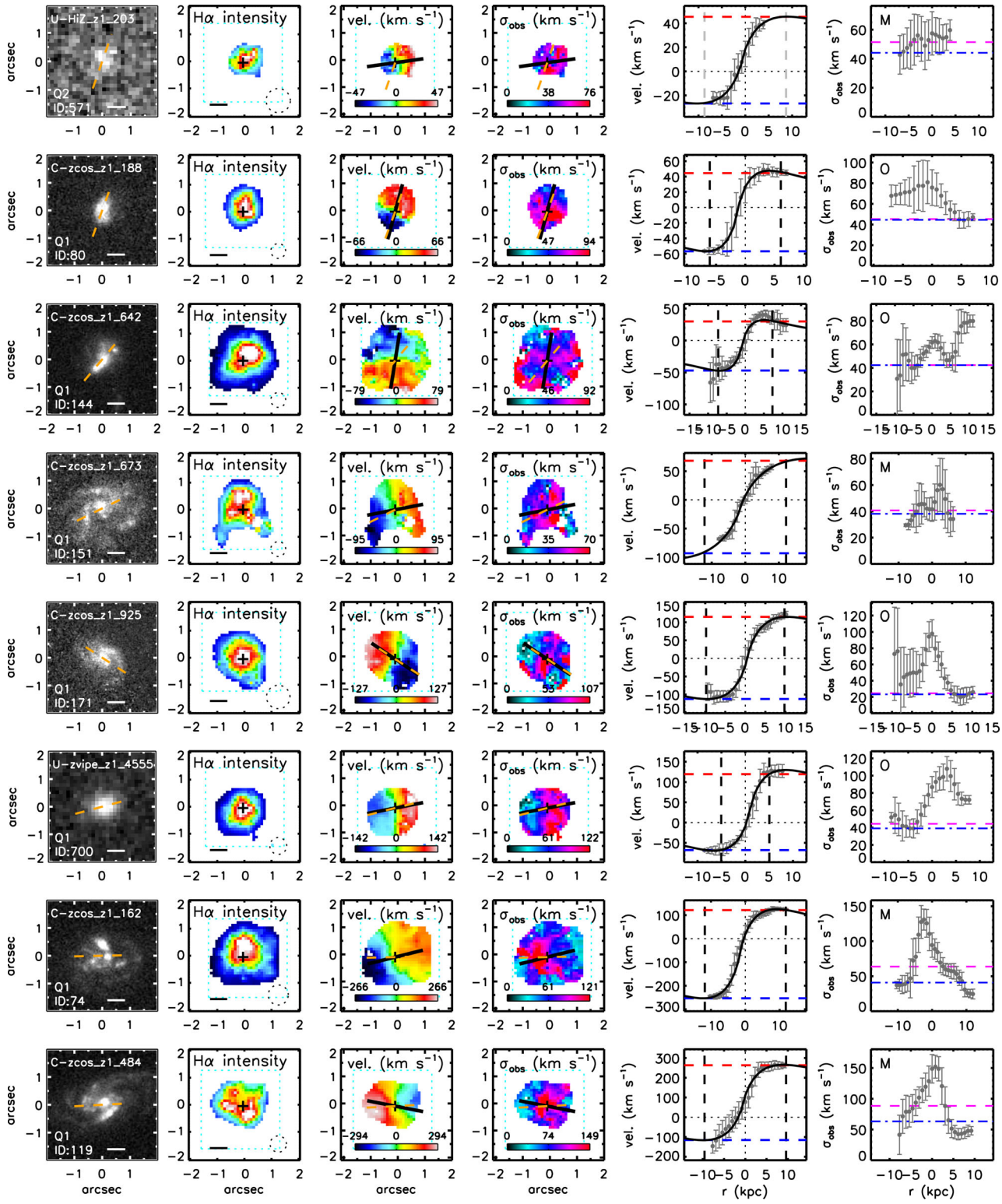

Figure 2. Example data for eight galaxies in the KROSS sample (a complete set of figures is available in the online version of Harrison et al. 2017), arranged by increasing stellar mass from top to bottom. Left to right: (1) Broad-band image with orange dashed line to represent PA_{im}. We also display the quality flag (see Section 3.7) and a 5 kpc scale bar. (2) Hα intensity map with cross to mark the continuum centre and dashed circle to represent the seeing FWHM. (3) Hα velocity map with dashed orange line to represent PA_{im} and solid black line to represent PA_{vel}. (4) Observed Hα velocity dispersion map with lines as in panel 3. (5) Rotation curve extracted along a 0.7 arcsec wide 'slit' of PA_{vel}. The solid curve describes a disc model which we use to find the rotation velocity at $\pm 3.4\,R_d$ (dashed vertical lines). To estimate v_{obs}, we take the average of these two values (horizontal dashed lines). (6) Observed velocity dispersion profile extracted along PA_{vel}, with dashed line to represent $\sigma_{0,obs}$ as measured in the outskirts of the disc (O) or from the median of all pixels (M). The dot–dashed line shows the same value corrected for beam smearing (σ_0). In general, as the stellar mass of the galaxy increases, we see a larger peak in the dispersion profile due to beam smearing.

Downloaded from https://academic.oup.com/mnras/article-abstract/474/4/5076/4655192 by University of Queensland Library user on 07 February 2020

error bar associated with each point represents all variation within the 'slit'.

To minimize the impact of noise on our measurements, we fit each rotation curve as an exponential disc (Freeman 1970) of the form:

$$v(r)^2 = \frac{r^2 \pi G \mu_0}{R_\mathrm{d}}(I_0K_0 - I_1K_1) + v_\mathrm{off}, \quad (2)$$

where r is the radial distance, μ_0 is the peak mass surface density, R_d is the disc radius, and I_nK_n are the Bessel functions evaluated at $0.5r/R_\mathrm{d}$. The final parameter, v_off, is the velocity measured at the centre of the galaxy and we apply this offset to the rotation curve before making measurements. We model each galaxy in this way with the intention of interpolating the data to obtain a more robust measurement. However, for 13 per cent of galaxies we must extrapolate (>0.4 arcsec; ∼3 kpc) beyond the data to evaluate the rotation velocity at the desired radius.

We measure the rotation velocities of our sample at two radii frequently used within the literature, $1.3R_{1/2}$ and $2R_{1/2}$ ($\approx 2.2R_\mathrm{d}$ and $3.4R_\mathrm{d}$ for an exponential disc). The first of these coincides with the peak rotation velocity of an ideal exponential disc, whilst the second probes outer regions of the galaxy, where we expect the rotation curve to have flattened. We refer to these measurements as $v_{2.2}$ and v_C, respectively. For each galaxy we convolve $R_{1/2}$ with the PSF of the KMOS observation[1] and extract velocities from the model rotation curve. At a given radius, our final measurement is half the difference between velocities on the blue and red side of the rotation curve. We account for beam smearing using the correction factors derived in Section 3.6. Finally, we correct for the inclination of the galaxy, as measured in Section 3.2.

A small subset of our sample (11 per cent) is unresolved in the KMOS data ('quality 4') or the broad-band imaging ('quality 3'). As such we are unable to extract rotation velocities for these galaxies from a rotation curve. Instead, we make estimates using the linewidth of the galaxy integrated spectrum and calibrate our results using galaxies for which both methods are available. From a sample of 586 Hα-detected galaxies, 433 are flagged as 'quality 1', 88 are 'quality 2', 31 are 'quality 3', and 34 are 'quality 4'. Only quality 1 and 2 sources are included in our results and discussion on the intrinsic velocity dispersions in Sections 4 and 5 (see also Section 3.7).

3.5 Velocity dispersions

Throughout our analysis, we assume that the intrinsic velocity dispersion is uniform across the disc (as in e.g. Epinat et al. 2012; Genzel et al. 2014; Simons et al. 2016). In the same way as we extract a rotation curve from the velocity map, we also extract a profile along the major kinematic axis of the velocity dispersion map. We use this profile to measure the observed dispersion, $\sigma_{0,\mathrm{obs}}$, by taking the median of values at either end of the kinematic axis $|R| > 2R_{1/2}$ and adopting whichever value is smallest (see Fig. 2). We assume the uncertainty on this measurement is the scatter of values included in the median. Evaluating $\sigma_{0,\mathrm{obs}}$ at radii far from the dynamical centre reduces any bias introduced by beam smearing (see Section 3.6), and measurements here should be close to the intrinsic dispersion.

Whilst this is our preferred method, 56 per cent of the resolved sample (307 galaxies) have insufficient S/N in the outer regions of the galaxy ($\pm 2R_{1/2}$) to be able to measure the dispersion in this way. Instead, we measure the median of all available pixels within the dispersion map. Once we apply the relevant beam smearing corrections derived in Section 3.6, we find that the $\sigma_{0,\mathrm{obs}}$ values from each method are in good agreement. In cases, where we can follow either approach the results are (on average) consistent to within 4 per cent, with ≈ 50 per cent scatter around this offset. We therefore assign an uncertainty of 50 per cent to measurements made using this second method. We do not estimate σ_0 for unresolved galaxies.

We note that Di Teodoro et al. (2016) derived intrinsic velocity dispersions using the KMOS data for 14 of the galaxies from our sample using their three-dimensional ^{3D}BARLO technique. 12/14 of their derived values agree with 2σ of our values but with ∼20 per cent lower velocity dispersions on average. Our method, whilst less complex, has the advantage that it can be uniformly applied to a range of data quality across a wide range of redshifts, allowing us to explore trends with redshift, mass, and SFR in very large samples (see Section 4.3).

3.6 Beam smearing corrections

Since our KMOS observations are seeing limited, we must consider the impact of the spatial PSF (the seeing) on our kinematic measurements. As IFU observations are convolved with the PSF, information from each spatial pixel is combined with that of neighbouring regions – a phenomenon known as 'beam smearing' (see e.g. Epinat et al. 2010; Davies et al. 2011; Burkert et al. 2016; Federrath et al. 2017a; Zhou et al. 2017). This acts to increase the observed velocity dispersion (particularly towards the dynamical centre) and to flatten the observed rotation curve, thereby reducing the observed velocity. In order to calibrate for these effects, we create a series of mock KMOS observations and derive correction factors that can be applied to the kinematic measurements. Our method for this correction is similar to that adopted by other authors (e.g. Burkert et al. 2016; Turner et al. 2017a) and we derive similar results. In Appendix B, we present full details of this investigation; however, the following is a brief summary.

To begin this process, we create a sample of $\sim 10^5$ model disc galaxies, with stellar masses and radii representative of the KROSS sample. We assume an exponential light profile and model the galaxy dynamics as the sum of a stellar disc plus a dark matter halo. An appropriate range of dark matter fractions is determined using results of the cosmological simulation suite 'Evolution and Assembly of GaLaxies and their Environments' (EAGLE; Crain et al. 2015; Schaye et al. 2015; Schaller et al. 2015). For simplicity, the intrinsic velocity dispersion (σ_0) is assumed to be uniform across the disc. From these properties, we can predict the intensity, linewidth, and velocity of the Hα emission at each position. We use this information to create an 'intrinsic' KMOS data cube for each galaxy.

To simulate the effects of beam smearing we convolve each wavelength slice of the cube with a given spatial PSF. We model a range of seeing conditions to match our KMOS observations. This forms the 'observed' data cube from which we extract dynamical maps (in the same way as for the observations) and measure $v_{\mathrm{C,obs}}$, $v_{2.2,\mathrm{obs}}$, and $\sigma_{0,\mathrm{obs}}$. Differences between the input values of the model and these 'observed' values then form the basis of our beam smearing corrections. The amplitude of the beam smearing is most sensitive to the size of the galaxy relative to the PSF. These corrections are best parametrized as a function of $R_\mathrm{d}/R_\mathrm{PSF}$, where R_PSF is half of the FWHM of the seeing PSF.

In Fig. 3, we show the ratio of the observed and intrinsic rotation velocity as a function of $R_\mathrm{d}/R_\mathrm{PSF}$. As expected, the larger the spatial

[1] That is, $R^2_{1/2,\mathrm{conv}} = R^2_{1/2} + \mathrm{FWHM}^2_\mathrm{PSF}$.

Downloaded from https://academic.oup.com/mnras/article-abstract/474/4/5076/4655192 by University of Queensland Library user on 07 February 2020

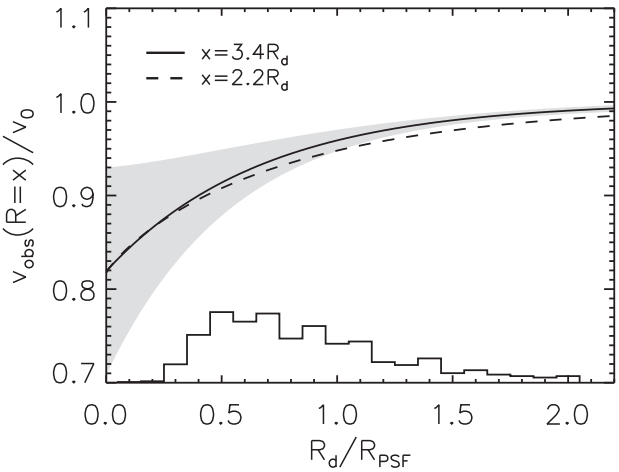

Figure 3. Beam smearing correction applied to measurements of the rotation velocity at radii of 3.4 and 2.2$R_{\rm d}$ ($v_{\rm C}$ and $v_{2.2}$, respectively), as a function of $R_{\rm d}/R_{\rm PSF}$. The shaded region represents the 1σ scatter of outcomes for $\sim10^5$ mock galaxies. Tracks show the median of these outcomes and are defined by equation (B6) and the parameters listed in Table B1. The histogram represents the $R_{\rm d}/R_{\rm PSF}$ distribution of the KROSS sample. Applying these beam smearing corrections to our data, we find a modest median velocity correction of $\xi_v = 1.07 \pm 0.03$ and range of $\xi_v = 1.0$–1.17.

PSF is compared to the disc, the more we underestimate the intrinsic velocity. Averaging over all stellar masses and inclinations, we find a median correction to $v_{\rm C}$ of $\xi_v = 1.07 \pm 0.03$, with a range of $\xi_v = 1.0$–1.17. Applying this correction acts to increase the median rotation velocity measurement by 4 km s^{-1}.

Similarly, the smaller the value $R_{\rm d}/R_{\rm PSF}$, the more we overestimate the intrinsic velocity dispersion. However, the impact of beam smearing on measurements of σ_0 also depends strongly on the velocity gradient across the disc (which is a function of both dynamical mass and inclination angle). In Fig. 4, we split corrections into four separate tracks as a function of $v_{\rm obs}$. The majority of galaxies in our sample (67 per cent) have observed rotation velocities of $v_{\rm obs} \leq 100$ km s^{-1}, so most corrections are made using the green and blue tracks of Fig. 4. The required adjustments are therefore relatively small. When using the velocity dispersions extracted from outer regions of the disc, we apply a median beam smearing correction of $\xi_\sigma = 0.97^{+0.02}_{-0.06}$. If a value is extracted from the median of the map, we apply a median factor of $\xi_\sigma = 0.8^{+0.1}_{-0.3}$. Applying these beam smearing corrections to KROSS data reduces the median velocity dispersion measurement by 9 km s^{-1}.

3.7 Definition of the final sample

In Section 2, we presented a mass- and colour-selected sample of 743 KROSS galaxies, 586 of which are detected in Hα. In Fig. 1, we show that this forms a representative sample of star-forming galaxies at this redshift ($z \approx 0.85$), in the context of the M_*–SFR 'main sequence'. With kinematic and morphological properties of these galaxies now established (e.g. Fig. 2), we make a number of additional cuts to the sample.

First, as in Harrison et al. (2017), we exclude 20 galaxies with line ratios of [N II]/H$\alpha > 0.8$ and/or a broad-line component to the Hα emission of $\geq$1000 km s^{-1}. These sources may have a significant active galactic nucleus (AGN) component or kinematics that are influenced by shocks (e.g. Kewley et al. 2013; Harrison et al. 2016). We also remove 30 sources that have multiple components in their broad-band imaging and/or IFU data. In doing so we hope to remove any potential major mergers. Finally, we exclude 'quality 4' and 'quality 3' sources that are unresolved or without a half-light radius measurement, respectively. This leaves a final sample of 472 galaxies.

Of this final sample, 18 per cent (84 galaxies) are classified as 'quality 2', owing to a fixed inclination angle or half-light radius measured from the rotation curve. For 49 per cent of the sample (231 galaxies), we are able to measure the velocity dispersion (σ_0)

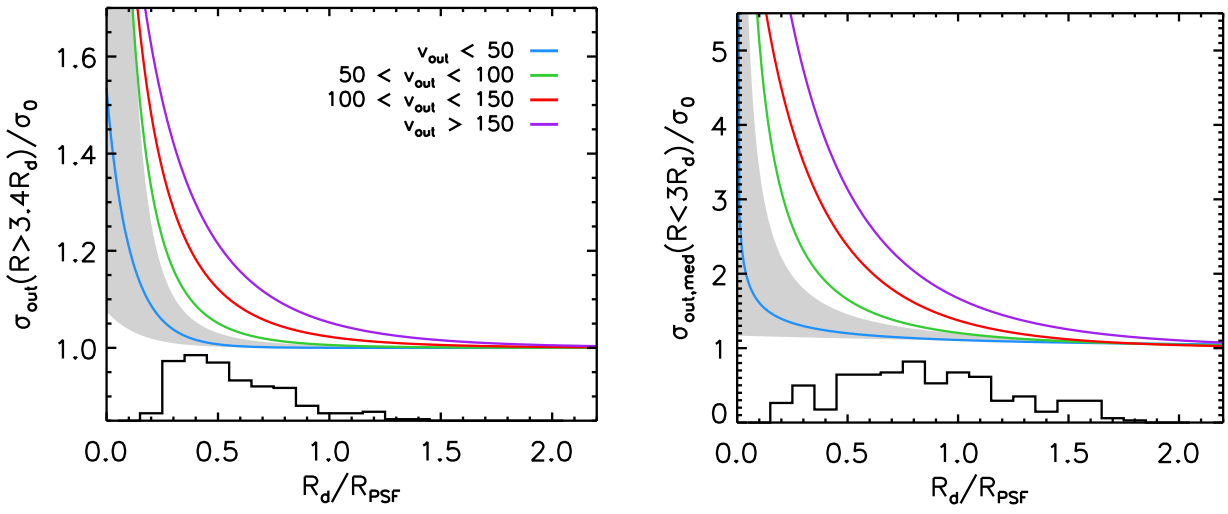

Figure 4. Beam smearing corrections for the velocity dispersion as a function of observed rotation velocity ($v_{\rm obs}$) and $R_{\rm d}/R_{\rm PSF}$. $R_{\rm PSF}$ is defined as half of the seeing FWHM and we assume an exponential disc such that $R_{\rm d} = R_{1/2}/1.678$. To derive these corrections, we create $\sim10^5$ model galaxies of various masses, radii, inclinations, dark matter fractions and intrinsic dispersions (σ_0; uniform across the disc), and simulate the effects of beam smearing for a seeing of 0.5–0.9 arcsec (see Section 3.6 and Appendix B). We fit a running median to the results of each velocity bin, with each track described by equation (B7) and the relevant parameters in Table B1. Shaded regions demonstrate the typical 1σ scatter of results in each bin, whilst the histograms represent the $R_{\rm d}/R_{\rm PSF}$ distribution of each subset. Note the different scales on the y-axes. Left: velocity dispersions measured in the outskirts ($R > 3.4R_{\rm d}$) of the dispersion profile, relative to the intrinsic value. We apply an average correction of $\xi_\sigma = 0.97^{+0.02}_{-0.06}$ to the KROSS sample. Right: dispersions measured as the median of all pixels. This method results in a greater overestimate of σ_0, with an average correction factor of $\xi_\sigma = 0.8^{+0.1}_{-0.3}$.

Downloaded from https://academic.oup.com/mnras/article-abstract/474/4/5076/4655192 by University of Queensland Library user on 07 February 2020

using data in the outer regions of the galaxy. For the remaining 51 per cent of cases (241 galaxies), we must measure the median of all IFU pixels and correct this value appropriately. As discussed in Section 3.5, these two methods are consistent; however, we attribute larger uncertainties to measurements made using the latter approach. The observed and beam smearing corrected velocity dispersions of each galaxy are listed in Table A1, and a full catalogue of galaxy properties is available online (see Appendix A).

4 RESULTS

In the previous section, we summarized the morphological and kinematic analysis of 586 Hα detected galaxies in the KROSS sample. After the removal of 114 sources that have either uncertain kinematic measurements, or show signs of a significant AGN component or merger event, we construct a final sample of 472 clean, well-resolved galaxies. In the following subsections, we present a detailed discussion of the velocity dispersion properties of this sample.

4.1 Velocity dispersions

We measure a median intrinsic velocity dispersion of $\sigma_0 = 43 \pm 1\,\mathrm{km\,s^{-1}}$ and a 16–84th percentile range of 27–61 $\mathrm{km\,s^{-1}}$. This median dispersion is lower than the $59 \pm 2\,\mathrm{km\,s^{-1}}$ previously reported for KROSS in Stott et al. (2016) due to a more rigorous beam smearing analysis, different measurement techniques, and further refinement of the kinematic sample (see Section 3 and Harrison et al. 2017). As discussed in Section 3.5, we measure the dispersion of each galaxy using one of two different methods. For approximately half of the sample, we measure σ_0 in outer regions of the disc ($|R| > 2R_{1/2}$), whilst for the remaining galaxies we calculate the median of all pixels. Since the ability to resolve kinematics in the outskirts is dependent on galaxy size and S/N, galaxies in the 'median' sample tend to be larger than those in the 'outskirts' sample (median half-light radii of 3.5 ± 0.1 kpc and 2.07 ± 0.08 kpc, respectively) and also more passive (median SFRs of $6.2 \pm 0.3\,\mathrm{M_\odot\,yr^{-1}}$ and $8.2 \pm 0.4\,\mathrm{M_\odot\,yr^{-1}}$). The velocity dispersions of this subset are also slightly higher, with a median σ_0 of $45 \pm 1\,\mathrm{km\,s^{-1}}$ as opposed to $41 \pm 1\,\mathrm{km\,s^{-1}}$.

In Fig. 5, we explore the relationship between stellar mass and velocity dispersion. We may expect these quantities to be related, since dispersions are important in measuring the dynamical support of galaxies, regardless of morphological type. For example, several authors have noted that the $S_{0.5}$ parameter [$S_{0.5} = (0.5\,v^2 + \sigma^2)^{1/2}$] correlates more strongly with stellar mass than rotational velocity alone (e.g. Kassin et al. 2007; Vergani et al. 2012; Cortese et al. 2014). Fig. 5 shows that before we account for beam smearing, the average velocity dispersion increases significantly with stellar mass. We measure a median $\sigma_{\rm obs}$ of $48 \pm 2\,\mathrm{km\,s^{-1}}$ in the lowest mass bin compared to $64 \pm 5\,\mathrm{km\,s^{-1}}$ in the highest. However as discussed in Section 3.6 (and extensively in Appendix B), a more massive galaxy is typically associated with a steeper velocity gradient across the disc (e.g. Catinella, Giovanelli & Haynes 2006) and hence stronger beam smearing. After we apply corrections as a function of $R_{\rm d}/R_{\rm PSF}$ and $v_{\rm obs}$ (Fig. 4) we no longer observe this trend and instead find the median σ_0 to be consistent across the four mass bins, with values between $42 \pm 2\,\mathrm{km\,s^{-1}}$ and $45 \pm 3\,\mathrm{km\,s^{-1}}$. If we consider only dispersion measurements made in the outskirts of the disc, values are almost identical – lower by a factor of 0.98 ± 0.03. Our results are consistent with σ_0 being almost independent of stellar mass over the range $\log(M_\star/\mathrm{M_\odot}) = 9.4$–$10.4$.

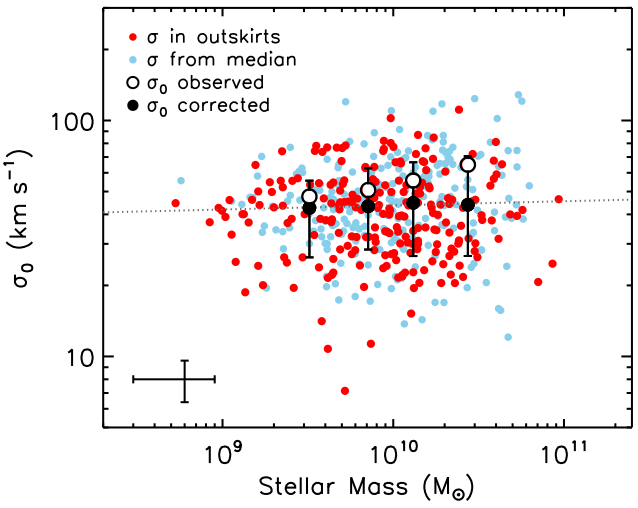

Figure 5. Beam smearing corrected velocity dispersion against stellar mass, with points coloured by the technique used to measure σ_0. Large black symbols show the median dispersion (and standard deviation) in bins of stellar mass. If we consider only measurements made in the outskirts of the disc these average values are systematically a factor of 0.98 ± 0.03 lower. Large open symbols show the median in each bin prior to the correction being applied. The large black points show that once we have accounted for the effects of beam smearing (see Section 3.6) we find σ_0 to be independent of $M_\star$. The dotted line is a fit to this trend.

4.2 Rotational support

To quantify the balance between rotational support and turbulence of the gas, we calculate the ratio between rotation velocity and velocity dispersion, $v_{\rm C}/\sigma_0$, for each of the KROSS galaxies. We find a median value of $v_{\rm C}/\sigma_0 = 2.6 \pm 0.1$ and a 16–84th percentile range of 0.9–5. We can use this ratio between rotation velocity and intrinsic dispersion to achieve a crude separation of 'dispersion dominated' and 'rotationally dominated' galaxies. Following e.g. Genzel et al. (2006), we adopt $v_{\rm C}/\sigma_0 = 1$ as a boundary between the two. By this definition, we find a rotationally dominated fraction of 83 ± 5 per cent, which suggests that the majority of star-forming galaxies at this redshift are already settled discs. The KROSS sample used for this work is slightly different to that presented in Harrison et al. (2017); for example, we include only 'quality 1' or 'quality 2' sources. However, our results are consistent, suggesting that this does not introduce a bias. Harrison et al. (2017) find a median value of $v_{\rm C}/\sigma_0 = 2.4 \pm 0.1$ and a rotationally dominated fraction of 81 ± 5 per cent. Despite a more detailed treatment of the beam smearing effects, our results are also consistent with the initial KROSS values derived in Stott et al. (2016).

In Fig. 6, we study how rotational support relates to stellar mass. Observations suggest that galaxies evolve hierarchically from disordered, dynamically hot systems to regularly rotating discs, with the most massive galaxies settling first (kinematic downsizing; e.g. Kassin et al. 2012; van der Wel et al. 2014; Simons et al. 2016, 2017). At a given redshift, it is expected that high-mass galaxies are more stable to disruptions due to gas accretion, winds, or minor mergers (e.g. Tacconi et al. 2013; Genzel et al. 2014). As such, we expect the most massive galaxies to exhibit the largest $v_{\rm C}/\sigma_0$ values. Fig. 6 demonstrates that this is indeed true for the KROSS sample, with median $v_{\rm C}/\sigma_0$ values of 1.3 ± 0.1 and 4.3 ± 0.3 in the lowest and highest mass bins, respectively, and 'dispersion dominated' systems more prevalent at low stellar mass. Since we observe no correlation between velocity dispersion and stellar mass, this increase must be

Downloaded from https://academic.oup.com/mnras/article-abstract/474/4/5076/4655192 by University of Queensland Library user on 07 February 2020

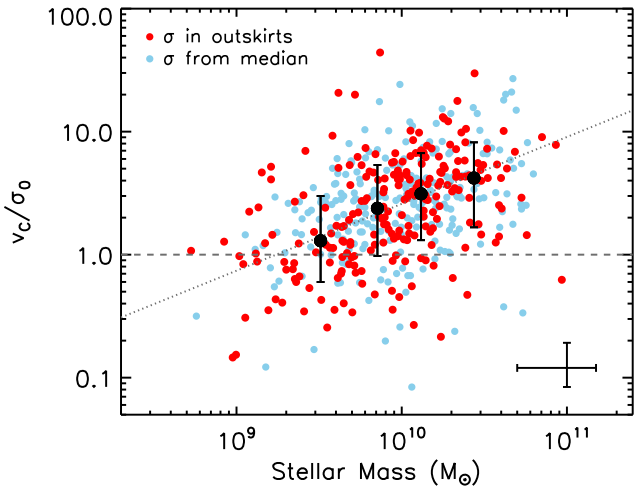

Figure 6. Ratio between inclination corrected rotational velocity (v_C) and intrinsic velocity dispersion (σ_0) against stellar mass. Fig. 5 shows that the average σ_0 is roughly the same in each mass bin; however, due to larger rotational velocities, we see an increase in v_C/σ_0 with increased stellar mass. We fit a trend to the median values in bins of increasing stellar mass (large black points) and plot this as a dotted line. The dashed line acts as a crude boundary between 'dispersion dominated' (below) and 'rotationally dominated' galaxies (above, ∼80 per cent of our sample). More massive galaxies appear to be more rotationally supported.

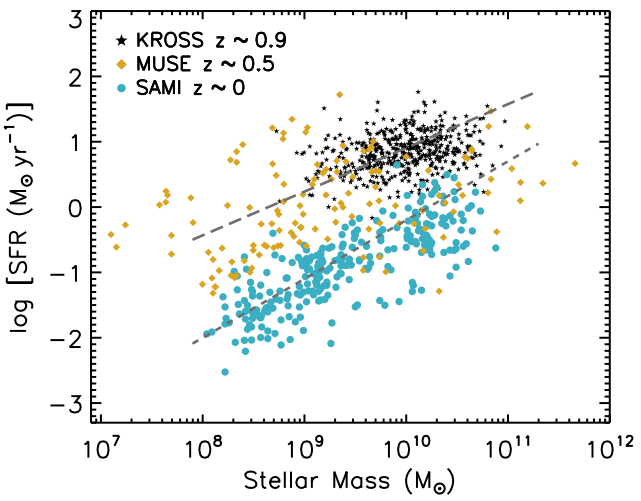

Figure 7. SFR versus stellar mass for the KROSS galaxies studied in this work (as in Fig. 1), and the MUSE and SAMI comparison samples discussed in Section 4.3. We overlay the star-forming 'main sequence' at $z = 0$ (Peng et al. 2010) and $z = 0.85$ (Speagle et al. 2014), which illustrate that the KROSS and SAMI samples are representative of typical star-forming galaxies at their respective redshifts. The MUSE sample are [O II] emitters serendipitously detected within observations of other targets; hence, these galaxies have a wide range of masses and SFRs.

a result of higher mass galaxies rotating more quickly. If $M_\star \propto v_C^2$, then we would expect v_C to increase by a factor of ∼3.2 over the mass range $\log(M_\star/M_\odot) = 9.4$–$10.4$. Indeed, for KROSS galaxies, we find a slope of ∼2.1 in the v_c versus mass plane, consistent with previous multiepoch galaxy studies (e.g. Harrison et al. 2017). This is consistent with our results in Fig. 6.

4.3 Trends between dispersion and stellar mass, SFR and redshift

To analyse the kinematics of KROSS galaxies in an evolutionary context, and to further explore how dispersion relates to other galaxy properties, we introduce comparison samples. In the 'IFU era', there are a multitude of kinematic surveys to choose from; however, it is often difficult to make comparisons since the techniques used, particularly for beam smearing corrections, can vary a great deal. In this subsection, we therefore consider only two additional samples, for which we can measure (and correct) σ_0 in a consistent way. In Section 4.4, we will study the average properties of a further five comparison samples.

4.3.1 SAMI sample

Our first comparison sample consists of 824 galaxies from the SAMI (Croom et al. 2012) Galaxy Survey. The goal of this survey is to provide a complete census of the spatially resolved properties of local galaxies ($0.004 < z < 0.095$; Bryant et al. 2015; Owers et al. 2017). SAMI is a front-end fibre feed system for the AAOmega spectrograph (Sharp et al. 2006). It uses a series of 'hexabundles' (Bland-Hawthorn et al. 2011; Bryant et al. 2014), each comprised of 61 optical fibres and covering a ∼14.7 arcsec field of view, to observe the stellar and gas kinematics of up to 12 galaxies simultaneously. Reduced SAMI data cubes have a 0.5 arcsec spatial sampling. A detailed description of the data reduction technique is presented in Sharp et al. (2015). The data used for this analysis were kindly provided by the SAMI team ahead of its public release. Details of the early data release can be found in Allen et al. (2015), and details of SAMI data release one can be found in Green et al. (2017).

In order to compare SAMI data to KROSS, we first make a series of cuts to the sample. In particular, the SAMI survey contains a number of early-type and elliptical galaxies with high Sérsic indices, high stellar masses, and low SFRs [hence, very low specific star formation rates (sSFRs)], which are not representative of the KROSS sample selection, that is to select typical star-forming galaxies for that epoch. We therefore remove galaxies from the SAMI sample with masses greater than $M_\star = 8\times\ 10^{10}\ M_\odot$ and a Sérsic index of $n > 2$ (since the derived σ_0 measurements for these galaxies are likely to be measuring different physical processes). We also remove sources that are unresolved at the SAMI resolution or have kinematic uncertainties greater than 30 per cent. This leaves a total of 274 galaxies with a median redshift $z \sim 0.04$ and median stellar mass $\log(M_\star/M_\odot) = 9.34 \pm 0.07$.

In Fig. 7, we plot SFR versus stellar mass for this sample. Stellar masses were estimated from $g - i$ colours and i-band magnitudes following Taylor et al. (2011), as described in Bryant et al. (2015). SFRs were estimated using Hα fluxes corrected for dust attenuation. Most SAMI galaxies are representative of the star-forming 'main sequence' at $z = 0$ (Peng et al. 2010), and hence at fixed stellar mass, SFRs are 30–50 times lower than for KROSS galaxies.

To measure rotation velocities and dispersions, we exploit the gas velocity maps, which use 11 strong optical emission lines including Hα and [O II]. From these maps, we make measurements using the same methods as for the KROSS sample (for an independent study of SAMI velocity dispersions, see Zhou et al. 2017). However, since the angular sizes of galaxies at this redshift are much larger, the field of view of SAMI often does not extend to $3.4R_d$. Instead, we use a radius of $2R_d$ and correct the derived quantities appropriately based on our modelling in Appendix B.

Downloaded from https://academic.oup.com/mnras/article-abstract/474/4/5076/4655192 by University of Queensland Library user on 07 February 2020

4.3.2 *MUSE sample*

For a second comparison, we exploit the sample of Swinbank et al. (2017), who study the kinematics of 553 [O II] emitters serendipitously detected in a series of commissioning and science verification observations using MUSE (Bacon et al. 2010), a panoramic IFU with 1 × 1 arcmin field of view and 0.2 arcsec spatial sampling. Science targets were largely extragalactic 'blank' fields or high-redshift galaxies and quasars. Due to the nature of the sample, sources span a wide range of redshifts, with $0.28 < z < 1.49$. To provide an intermediate between the redshifts of KROSS and SAMI, we restrict this sample to galaxies between $0.3 < z < 0.7$. In Swinbank et al. (2017), sources were classified as rotationally supported, merging, interacting or compact, based on their dynamics and optical morphologies. We choose to exclude major mergers and compact (unresolved) galaxies from our analysis, and also those that have poorly defined masses or optical radii. With the implementation of these cuts, our comparison sample consists of 133 galaxies with a median redshift of $z \sim 0.5$ and median stellar mass $\log(M_\star/\mathrm{M}_\odot) = 9.1 \pm 0.1$. Stellar masses were derived from M_H magnitudes, using the same method as for KROSS, and the SFRs calculated using dust-corrected [O II] fluxes. Fig. 7 shows that since the selection is based only on [O II] flux, galaxies are scattered within the $M_\star$–SFR plane and it is more difficult than for SAMI and KROSS to identify a 'main sequence'; however, SFRs are generally between those of the $z \sim 0$ and $z \sim 0.9$ samples.

Swinbank et al. (2017) extract rotation velocities at radii of $3R_\mathrm{d}$, and we apply the beam smearing corrections derived in Section 3.6 to these values. Velocity dispersions are calculated by first applying a pixel-by-pixel $\Delta v/\Delta R$ correction to the map (i.e. subtracting the average shear across the pixel in quadrature), and then finding the median of all pixels outside of the seeing PSF. This beam smearing method is very similar to that for KROSS and so no additional corrections are applied in our comparison.

4.3.3 *Dispersion properties*

In Fig. 8, we plot the relationships between velocity dispersion and stellar mass, SFR, and sSFR. In the upper panels, the error bars show the 1σ scatter in the distributions. In the lower panels, the errors show the uncertainty in the median values, measured from a bootstrap resample (with replacement) of the values. At a given redshift, there appears to be at most only a weak trend between stellar mass and gas velocity dispersion. This is consistent with the results of other high-redshift kinematic studies (e.g. Kassin et al. 2012; Wisnioski et al. 2015; Simons et al. 2017; Turner et al. 2017a). We observe a larger trend of increasing dispersion with stellar mass for the SAMI sample than for KROSS (where any change is not significantly detected) and MUSE; however, this is still only a $12 \pm 5\,\mathrm{km\,s^{-1}}$ change associated with a factor ∼100 increase in stellar mass. Such a small trend cannot be ruled out for the KROSS sample. What is more apparent is an increase in σ_0 with redshift. In the lower left-hand panel of Fig. 8, we show that for a fixed stellar mass the average velocity dispersions of KROSS and MUSE galaxies are ∼50 per cent higher than for the SAMI sample at $z \sim 0$ (see also Zhou et al. 2017). As we show below, the apparent increase in σ_0 from $z \sim 0.5$ to $z \sim 0.85$ in the lower left-hand panel is not apparent when the samples are matched in mass-normalized SFRs.

In Fig. 8, we also investigate how dispersion is affected by global SFR. Whilst there is little overlap between the three samples, the three samples combined indicate a weak trend of increasing dispersion with increasing SFR. Although we observe only a 20–25 $\mathrm{km\,s^{-1}}$ change (a factor of ∼2 increase) in σ_0 across three orders of magnitude in SFR, this result is consistent with a number of previous studies (e.g. Lehnert et al. 2009, 2013; Green et al. 2010, 2014; Le Tiran et al. 2011; Moiseev, Tikhonov & Klypin 2015). Typically, a weak trend is observed below $10\,\mathrm{M}_\odot\,\mathrm{yr}^{-1}$ and it is only above this threshold that there is a strong increase in velocity dispersion with SFR. Few KROSS galaxies fit this criteria. Several authors have interpreted the relationship between star formation and dispersion as evidence of feedback driven turbulence; however, Krumholz & Burkhart (2016) argue that turbulence driven by disc instability would manifest in a similar way. In Section 5, we investigate whether it is possible to distinguish between these two different scenarios using our data set.

One way to normalize for differences in SFR and mass between samples is to plot the sSFR (SFR/$M_\star$). In the top right-hand panel of Fig. 8, we plot velocity dispersion against sSFR and find that for all three samples σ_0 is remarkably constant. There is a variation of less than $5\,\mathrm{km\,s^{-1}}$ across an order of magnitude in sSFR for KROSS and SAMI, and of less than $10\,\mathrm{km\,s^{-1}}$ across three orders of magnitude for the MUSE sample. In the panel below this, we study the relationship between velocity dispersion and redshift, calculating the median of each sample for a fixed range in sSFR. It is difficult to make a robust comparison since the SAMI galaxies tend to have a much lower sSFR; however, there appears to be a systematic increase in dispersion with redshift. We see an increase of ∼50 per cent between $z \sim 0$ and 0.9.

4.4 Dynamics in the context of galaxy evolution

Kinematic studies at high redshift suggest that star-forming galaxies at early times were dynamically 'hot', with velocity dispersions much larger than those observed for discs in the local Universe. In this section, we examine how the KROSS galaxies fit within a wider evolutionary context, comparing their dynamics to those of the SAMI and MUSE samples discussed in Section 4.3 and five additional comparison samples between $0 < z < 2.5$. For this comparison, we include data from the GHASP [Epinat et al. 2010; $\log(M_\star^{\mathrm{avg}}/\mathrm{M}_\odot) = 10.6$], KMOS$^{3\mathrm{D}}$ [Wisnioski et al. 2015; $\log(M_\star^{\mathrm{avg}}/\mathrm{M}_\odot) = 10.7$ and 10.9 for the $z \sim 1$ and 2 samples, respectively], MASSIV [Epinat et al. 2012; $\log(M_\star^{\mathrm{avg}}/\mathrm{M}_\odot) = 10.5$], SIGMA [Simons et al. 2016; $\log(M_\star^{\mathrm{avg}}/\mathrm{M}_\odot) = 10.0$], and SINS [Cresci et al. 2009; Newman et al. 2013; $\log(M_\star^{\mathrm{avg}}/\mathrm{M}_\odot) = 10.6$] surveys. These are all large samples ($\gtrsim$50 galaxies) of 'typical' star-forming galaxies, with SFRs representative of the main sequence at a particular redshift. Beam smearing of the intrinsic velocity dispersion has been accounted for in each sample, either through disc modelling or post-measurement corrections. With the exception of GHASP (Fabry-Pérot) and SIGMA (MOSFIRE), these are IFU-based studies.

In calculating average dispersion and v_C/σ_0 values, we note that different authors adopt different approaches. For example, Wisnioski et al. (2015) consider only 'discy' galaxies within the KMOS$^{3\mathrm{D}}$ sample, selected based on five criteria including $v_\mathrm{C}/\sigma_0 > 1$, a smooth gradient within the velocity map ('spider diagram'; van der Kruit & Allen 1978), and a dispersion that peaks at the position of the steepest velocity gradient. However, it is difficult to isolate a similar subset for each of the samples discussed here. For example, Epinat et al. (2010) have shown that up to 30 per cent of rotators may be misclassified if a velocity dispersion central peak is required. Low spatial resolution may also lead kinematically irregular galaxies to be misidentified as rotators (e.g. Leethochawalit et al. 2016).

Downloaded from https://academic.oup.com/mnras/article-abstract/474/4/5076/4655192 by University of Queensland Library user on 07 February 2020

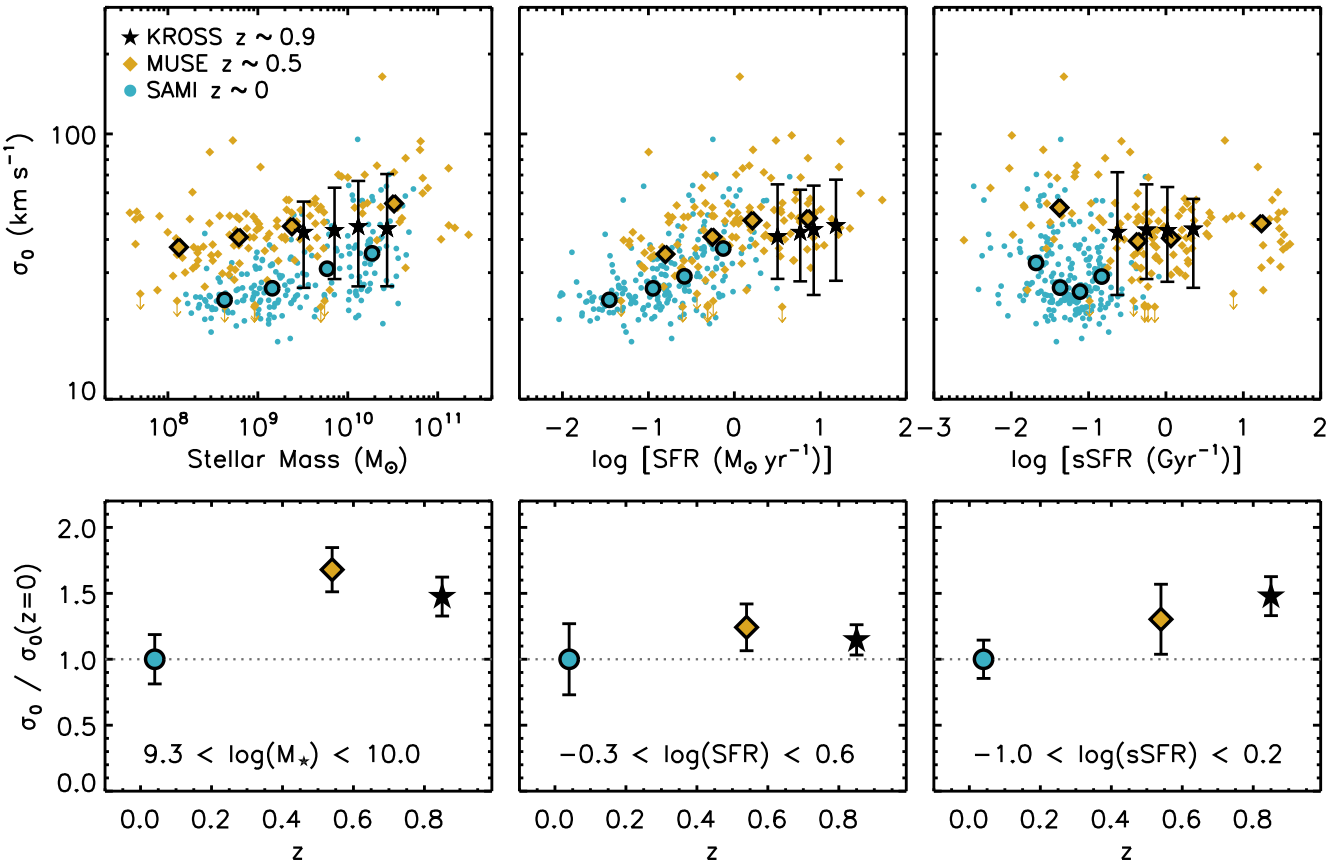

Figure 8. Top: Trends between velocity dispersion (σ_0) and a selection of non-kinematic properties for KROSS galaxies (this study) and the two comparison samples outlined in Section 4.3. For the SAMI and MUSE samples, we plot properties of individual galaxies and overlay medians within a series of x-axis bins (each containing 25 per cent of the sample). For clarity, for KROSS galaxies we show only the median values, with error bars to represent the 1σ scatter. Top left: Velocity dispersion versus stellar mass. At any given redshift, there is no strong correlation between dispersion and stellar mass; however, higher redshift galaxies appear to have larger dispersions. Top middle: Velocity dispersion versus SFR. Whilst there is little overlap in SFR between the three samples, we observe a weak trend of increasing dispersion with increasing SFR. Top right: Velocity dispersion versus sSFR. For individual samples, we see no significant trend between dispersion and sSFR, but again there appears to be an increase with redshift. Bottom: Velocity dispersion versus redshift, relative to the SAMI sample. We calculate the median dispersion of each sample over the same range in (left to right) $M_\star$, SFR, or sSFR and plot these values as a function of redshift. In these plots, the error bars denote the bootstrap error on the median. For fixed stellar mass or fixed sSFR, we see a weak trend of increasing dispersion with redshift. For fixed SFR, the values are consistent within the uncertainties.

In the left-hand panel of Fig. 9, we plot the median, mean, and distribution of velocity dispersion measurements for each of the eight samples, as a function of redshift. As has been noted before, there is a gradual increase in the average velocity dispersion from $\sim$25 km s^{-1} at $z = 0$ to $\sim$50 km s^{-1} at $z = 2$. At $z \sim 1$, Wisnioski et al. (2015) report an average of $\sigma_0 = 25 \pm 5$ km s^{-1} for the KMOS^{3D} sample, whereas for KROSS we measure a median of $\sigma_0 = 43.2 \pm 0.8$ km s^{-1}. We attribute this difference to the samples used to calculate the median (also see Di Teodoro et al. 2016), with stricter criteria applied to isolate 'discy' galaxies. Applying a series of criteria that directly or indirectly isolate 'discy' galaxies has the effect of removing the higher velocity dispersion sources and selecting the most dynamically mature galaxies, with such samples being increasingly less representative of the overall star-forming population with increasing redshift (e.g. see Turner et al. 2017b for a discussion). We restrict the KROSS, SAMI, and MUSE samples to 'rotationally dominated' galaxies, towards being more consistent with their sample, and plot the medians as open symbols. For KROSS, we find a reduced median of $\sigma_0 = 36 \pm 2$ km s^{-1}, which is in better agreement.

There has been much discussion as to which physical processes drive the observed evolution of velocity dispersion with redshift. We explore the theoretical arguments in Section 5. However, in this subsection we follow the analysis of Wisnioski et al. (2015), interpreting the results of Fig. 9 in the context of a rotating disc with a gas fraction and sSFR that evolve as a function of redshift. In this simple model, the gas fraction of the disc is defined as Tacconi et al. (2013):

$$f_{\rm gas} = \frac{1}{1 + (t_{\rm dep}{\rm sSFR})^{-1}}, \quad (3)$$

where the depletion time evolves as $t_{\rm dep}({\rm Gyr}) = 1.5 \times (1 + z)^{\alpha}$. From molecular gas observations of $z = 1$–3 galaxies, Tacconi et al. (2013) measure $\alpha = -0.7$ to -1.0; however, the analytic models of Davé, Finlator & Oppenheimer (2012) predict $\alpha = -1.5$. Here, $\alpha = -1.0$ is adopted as a compromise. The cosmic sSFR is assumed to follow the evolution described in Whitaker et al. (2014), where

$${\rm sSFR}(M_\star, z) = 10^{A(M_\star)}(1 + z)^{B(M_\star)}. \quad (4)$$

Downloaded from https://academic.oup.com/mnras/article-abstract/474/4/5076/4655192 by University of Queensland Library user on 07 February 2020

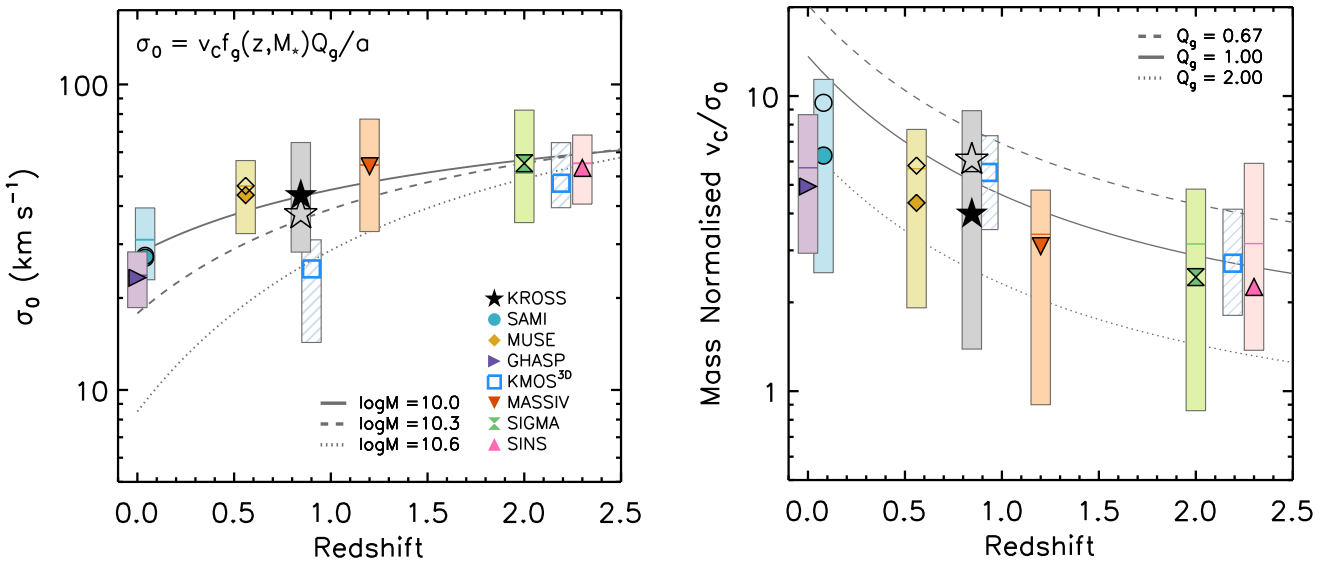

Figure 9. Velocity dispersion and (mass normalized) ratio between rotational velocity and velocity dispersion as a function of redshift. Alongside our results for KROSS, we include the SAMI and MUSE samples described in Section 4.3 and five samples from the literature, chosen such that our measurements and beam smearing corrections are comparable. Filled symbols represent the median, horizontal lines the mean, and vertical bars the 16–84th percentile range. Symbols for KMOS^{3D} represent the median of 'rotationally dominated' galaxies only, and the shaded bars represent the central 50 per cent of the distribution. We plot open symbols for the KROSS, SAMI, and MUSE samples for comparison, showing the median of galaxies with $v_C/\sigma_0 > 2$. Left: Intrinsic velocity dispersion as a function of redshift, with a simple Toomre disc instability model (equations 3–5) plotted for $\log(M_\star) = 10.0$–10.6. The model appears to provide a good description of the data. Right: v_C/σ_0 as a function of redshift, with a simple disc model overlaid for $Q_g = 0.67$–2. Values have been normalized to a stellar mass of $\log(M_\star) = 10.5$. The data are broadly consistent with the model, and we observe a decrease in v_C/σ_0 with redshift. For KMOS^{3D}, data were only available for 'rotationally dominated' galaxies. If we consider the same subsample of KROSS, our results are similar.

This sSFR relation was derived to fit UV+IR SFRs of ∼39 000 galaxies in the redshift range of $0.5 < z < 2.5$ (3D-*HST* survey; Momcheva et al. 2016). Finally, the Toomre disc stability criterion for a gas disc (Q_g; Toomre 1964) can be rewritten in terms of f_{gas} (see Glazebrook 2013) as

$$\frac{v_C}{\sigma_0} = \frac{a}{f_{gas}(z, M_\star)Q_g}, \quad (5)$$

where $a = \sqrt{2}$ for a disc of constant rotational velocity. In the left-hand panel of Fig. 9 we overplot the relationship between velocity dispersion and redshift derived for a range of stellar masses. Following the approach of Turner et al. (2017a), the value of $Q_g v_C$ is set such that the $\log(M_\star/M_\odot) = 10.0$ track is normalized to fit the median dispersion of the KROSS sample. For a marginally stable thin gas disc ($Q_g = 1$), this requires a model rotation velocity of $v_C = 150\,\mathrm{km\,s^{-1}}$. By comparison, we measure a median velocity for the KROSS sample of $v_C = 118 \pm 4\,\mathrm{km\,s^{-1}}$. This simple model appears to provide a reasonable description of the data.

Whilst these tracks provide useful guidance, we would typically expect the average rotation velocity, and not just the gas fraction, to vary as a function of mass. To eliminate this dependency, in the right-hand panel of Fig. 9 we show how v_C/σ_0 is expected to evolve for a galaxy of stellar mass $\log(M_\star/M_\odot) = 10.5$ and Toomre parameter of $Q_g = 0.67$, 1, or 2. These are the critical values for a thick gas disc, thin gas disc, and stellar-plus-gas disc, respectively (see e.g. Kim & Ostriker 2007). We then plot the median, mean, and distribution of v_C/σ_0 values for the eight samples, normalizing each to the stellar mass of the models. These correction factors range between 0.7 and 3.0 with a median of 1.1 ± 0.2, with the largest applied to the SAMI sample [median $\log(M_\star/M_\odot) = 9.3$].

The data follow the general trend described by the model, with a decrease from $v_C/\sigma_0 \sim 6$ at $z = 0$ to $v_C/\sigma_0 \sim 2$ at $z = 2$. This general trend is consistent with the results of Turner et al. (2017a).[2] The model predicts that this is due to higher gas fractions in galaxies at early times. Again we highlight the effect of restricting the KROSS, SAMI, and MUSE samples to 'rotationally dominated' galaxies, with open symbols. For KROSS, the median *mass-weighted* v_C/σ_0 increases from 3.9 ± 0.2 to 6.1 ± 0.2. This result is consistent with KMOS^{3D} at $z \sim 1$, who find $v_C/\sigma_0 = 5.5$ (Wisnioski et al. 2015).

The right-hand panel of Fig. 9 appears to suggest a weak trend between Toomre Q_g and redshift. We caution that Q_g is a galaxy averaged value, sensitive to systematics, and is therefore only a crude measure of disc stability. However to explore this potential trend, in Fig. 10 we plot the 'best-fitting' Toomre parameter required to fit the observed median v_C/σ_0 for each of the samples, given their respective redshifts and stellar masses. To calculate error bars, we propagate the typical uncertainties associated with measurements of the dynamics and stellar mass. Within the framework of this model, we find that lower redshift samples are associated with higher average values of Q_g.

This increase in Q_g is consistent with recent numerical simulations (Danovich et al. 2015; Lagos et al. 2017) and observational studies (Obreschkow et al. 2015; Burkert et al. 2016; Harrison et al. 2017; Swinbank et al. 2017) that suggest that the specific angular momentum of galaxy discs (j_s) increases with time. An increase in angular momentum would act to increase the global Q parameter, stabilizing discs against fragmentation. Obreschkow et al. (2015) and Swinbank et al. (2017) suggest this is likely what drives the morphological transition between clumpy, irregular discs

[2] We note that for the GHASP sample, Turner et al. (2017a) use the results from Epinat et al. (2008), whereas we use the results presented in Epinat et al. (2010).

Downloaded from https://academic.oup.com/mnras/article-abstract/474/4/5076/4655192 by University of Queensland Library user on 07 February 2020

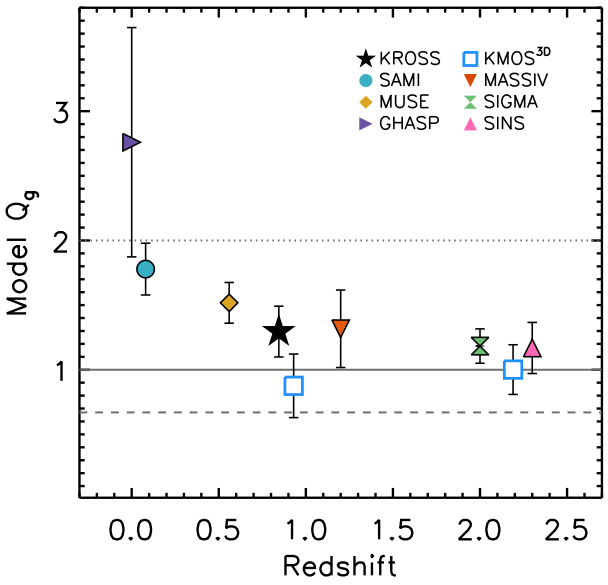

Figure 10. Inferred Toomre Q versus redshift for KROSS and comparison samples. Assuming a simple disc instability model (see Section 4.4 and equations 3–5), we calculate the Toomre Q parameter required to fit the average v_C/σ_0 observed for KROSS and various comparison samples, given their respective redshifts and stellar masses. Error bars reflect typical uncertainties associated with measurements of the stellar mass and dynamics. The lines overplotted at $Q_g = 0.67$, 1, and 2 represent the critical values for a thick gas disc, thin gas disc, and stellar-plus-gas disc, respectively. We find that higher redshift samples are best fit by lower values of Q, which would suggest that these galaxies are more unstable discs.

at high redshift, and the bulge-dominated galaxies with thin spiral discs we see today. Obreschkow et al. (2015) propose that $Q \propto (1 - f_g) j_s \sigma_0$. Hence, if the gas fraction decreases by a factor of 4 between $z \sim 2$ and $z \sim 0$ (e.g. Tacconi et al. 2010; Saintonge et al. 2013; Genzel et al. 2015), and the dispersion by a factor of 2 (Fig. 9), then a factor of ∼2.6 increase in specific angular momentum would achieve the increase in disc stability suggested by Fig. 10.

The 'toy model' described in this section is a useful tool, allowing us to interpret the evolution of galaxy dynamics in terms of gas fraction and disc instability. However, it provides little information about the physical mechanisms involved. For a deeper understanding, we must combine our observations with theoretical predictions.

5 THE ORIGIN OF DISC TURBULENCE: STAR FORMATION FEEDBACK VERSUS GRAVITATIONAL INSTABILITY

Although the simple framework in Section 4.4 provides an adequate description of the data, other – more detailed – physical models have been proposed to explain the origin of these high turbulent motions. Turbulence in the ISM decays strongly within the disc crossing time (∼15 Myr; Mac Low et al. 1998; Stone et al. 1998; Mac Low 1999), so a source of energy is clearly required to maintain disorder in the system. What this might be is the subject of active discussion; however, a large and well-selected sample such as KROSS may be able to provide useful constraints. In this section, we consider whether our data can be used to distinguish between two potential disc turbulence mechanisms.

One model is that the high level of turbulence is driven by stellar feedback. Supernovae and winds inject energy into the ISM, and several authors have identified a correlation between velocity dispersion and SFR, either on global or spatially resolved scales (e.g. Lehnert et al. 2009, 2013; Green et al. 2010, 2014; Le Tiran et al. 2011; but see Genzel et al. 2011). However, simulations including only stellar feedback struggle to reproduce these large observed dispersions (Joung, Mac Low & Bryan 2009; Shetty & Ostriker 2012; Kim, Ostriker & Kim 2013, 2014) without high rates of momentum injection (e.g. Hopkins, Quataert & Murray 2011; Hopkins et al. 2014).

An alternative framework is a clumpy, gas-rich disc fed by rapid accretion from the intergalactic medium (IGM). Whilst accretion of material *on to* the disc appears in itself insufficient to drive large velocity dispersions (e.g. Elmegreen & Burkert 2010; Hopkins, Kereš & Murray 2013, though see Klessen & Hennebelle 2010), simulations suggest that gravitational instabilities may induce high levels of turbulence (e.g. Aumer et al. 2010; Bournaud et al. 2010, 2014; Ceverino et al. 2010; Goldbaum et al. 2015; Goldbaum, Krumholz & Forbes 2016) that can be sustained by the accretion of mass *through* the disc. As mass is transported inwards, the dispersion, and hence Q, is increased. Decay of this turbulence then acts to reduce Q, and eventually the disc saturates at a state of marginal stability. Several authors have considered whether gravitational interactions between clumps (formed via fragmentation of the disc) may also help to generate turbulence (Dekel et al. 2009; Aumer et al. 2010).

Krumholz & Burkhart (2016) noted that whilst the origins of disc turbulence have been explored in detail from a theoretical point of view, there had previously been few direct observational tests. To address this, the authors formulated two simple models – describing gravity-driven turbulence and feedback-driven turbulence – which could be used to make observational predictions. We outline each of these below.

5.1 Gravity-driven model

For a model in which turbulence is driven by gravitational instabilities in the gas, Krumholz & Burkhart (2016) adopt expressions for gas surface density (Σ) and velocity dispersion (σ) derived for the 'steady-state configuration' described in Krumholz & Dekel (2010). Within this framework, the gas surface density depends on the total Toomre Q parameter (as opposed to that of the gas or stars alone; i.e. Q_g or $Q_\star$), since the turbulence is driven by a global instability of the disc. The Wang & Silk (1994) approximation is adopted such that $Q^{-1} = Q_g^{-1} + Q_\star^{-1}$ and

$$Q \approx \frac{a v_C \sigma f_g}{\pi G r \Sigma}, \quad (6)$$

with $a = \sqrt{2}$. Here, v_C is the rotational velocity measured at a radius of r, σ is the velocity dispersion, and Σ is the gas surface density. It is expected that the disc self-regulates at $Q \approx 1$. Star formation is then added to the model assuming a so-called Toomre regime (Krumholz, Dekel & McKee 2012), in which the 'entire ISM is a single star-forming structure'. This is a key distinction between this model and the feedback-driven model discussed below. Together, these

Downloaded from https://academic.oup.com/mnras/article-abstract/474/4/5076/4655192 by University of Queensland Library user on 07 February 2020

assumptions lead to a SFR that depends on the velocity dispersion as

$$\mathrm{SFR} = \frac{16}{\pi}\sqrt{\frac{\phi_\mathrm{P}}{3}}\left(\frac{\epsilon_\mathrm{ff} v_\mathrm{C}^2}{G}\ln\frac{r_1}{r_0}\right) f_\mathrm{g}^2\sigma, \quad (7)$$

where ϵ_ff is the SFR per freefall time, f_g is the gas fraction, ϕ_P is a constant to account for the presence of stars, and $\ln(r_1/r_0)$ relates to the radial extent of the disc.

5.2 Feedback-driven model

One way for analytic models to achieve large velocity dispersions via stellar feedback is to assume that the star formation efficiency within giant molecular clouds (GMCs) is closely coupled to the Toomre parameter of the gas disc (Q_g). Activity on the scale of GMCs is driven by self-gravity of the gas clouds and hence feedback-driven models do not require a global $Q \approx 1$ provided $Q_\mathrm{g} \approx 1$. The expression for the gas Toomre parameter is similar to equation (6),

$$Q_\mathrm{g} \approx \frac{a v_\mathrm{C}\sigma}{\pi G r \Sigma}. \quad (8)$$

In their model, Krumholz & Burkhart (2016) adopt the star-forming relation of Faucher-Giguère, Quataert & Hopkins (2013), which balances the momentum per unit mass ($p_\star/m_\star$) injected by feedback against the gas surface density squared. This results in a relationship between SFR and velocity dispersion of

$$\mathrm{SFR} = \frac{8\sqrt{2}\phi v_\mathrm{C}^2}{\pi G Q_\mathrm{g}\mathcal{F}}\left(\ln\frac{r_1}{r_0}\right)\left(\frac{p_\star}{m_\star}\right)^{-1}\sigma^2, \quad (9)$$

where ϕ and $\mathcal{F}$ are constants associated with various model uncertainties. There are two key differences between this and the gravity-driven model. First, since stellar feedback depends on the amount of gas unstable to gravitational collapse, we assume $Q_\mathrm{g} \approx 1$ and not $Q \approx 1$. As a consequence, equation (9) does not depend on f_g. Secondly, the SFR is more strongly dependent on the velocity dispersion than for a gravity-driven model. For turbulence to balance gravity in the ISM, the SFR density must be proportional to the gas surface density squared. Since $\Sigma \propto \sigma$ for constant Q_g, we therefore obtain $\mathrm{SFR} \propto \sigma^2$, as opposed to $\mathrm{SFR} \propto \sigma$ for the gravity-driven model (equation 7).

5.3 Comparison of models to observations

KROSS offers a large and representative sample of ∼500 star-forming galaxies, with velocity dispersions measured and corrected for beam smearing in a consistent way. This is an ideal opportunity to test predictions of the aforementioned analytic models. Krumholz & Burkhart (2016) compared observational data to their models of feedback-driven turbulence and gravity-driven turbulence. As shown by Krumholz & Burkhart (2016), most of the diagnostic power in differentiating between the gravity-driven and feedback-driven turbulence models is from galaxies with the highest SFR (above SFRs of $\gtrsim 50\,\mathrm{M_\odot\,yr^{-1}}$, the predictions for the amount of turbulence from the two models most rapidly diverge). However, whilst these data cover many orders of magnitude in SFR, it consists of samples of differing selection criteria, redshift, and data quality. In this section, we attempt to use our sample to test these predictions, although we note that the majority of our samples have SFRs in the range of 2–30 $\mathrm{M_\odot\,yr^{-1}}$.

5.3.1 Model tracks

In Fig. 11, we plot velocity dispersion against SFR for KROSS and overlay the models of Krumholz & Burkhart (2016).[3] In the top left-hand panel, we plot trends for a feedback-driven model, adopting the median rotation velocity of the sample ($\sim 120\,\mathrm{km\,s^{-1}}$) and Toomre $Q_\mathrm{g} = 0.5$, 1.0, and 2.5. These tracks show only a moderate increase in velocity dispersion with SFR, which is consistent with our data. For KROSS, galaxies in the lower quartile of SFR have a median dispersion of $42 \pm 2\,\mathrm{km\,s^{-1}}$ and those in the upper quartile have a median of $45 \pm 2\,\mathrm{km\,s^{-1}}$. The dispersion predicted by the model is much more sensitive to rotation velocity than Q_g. The shaded region around the $Q_\mathrm{g} = 1.0$ track shows the effect of adjusting the rotation velocity of the model by $20\,\mathrm{km\,s^{-1}}$, with larger values of v_C corresponding to smaller values of σ_0. The 68th percentile range for our sample is 44–204 $\mathrm{km\,s^{-1}}$, so it is possible that data points are consistent with a narrow range of Q_g if this effect dominates the scatter.

In the top right-hand panel of Fig. 11, we show trends for a gravity-driven model, with the same rotation velocity and gas fractions of $f_\mathrm{g} = 0.2$, 0.5, and 1.0. These models predict a sharp increase in velocity dispersion with SFR; however, this is not something seen in the data – we measure $\sigma_0 \geq 100\,\mathrm{km\,s^{-1}}$ for only a handful of KROSS galaxies. The expected velocity dispersion is very sensitive to the input rotation velocity and gas fraction. Despite our data being predominately low dispersion, this model may still be valid if the galaxies have a wide range in these other properties.

To eliminate this dependency on rotation velocity in the lower panels of Fig. 11, we plot $\log(v_\mathrm{C}^2\sigma_0^2)$ and $\log(v_\mathrm{C}\sigma_0^2)$ as a function of SFR for the feedback- and gravity-driven models, respectively. We note that low-dispersion galaxies ($\sigma_0 \leq 20\,\mathrm{km s^{-1}}$, scattered below the model trends) tend to be smaller compared to the seeing, and as such have larger beam smearing corrections (see Section 3.6). This sample has a median of $R_\mathrm{d}/R_\mathrm{PSF} = 0.35 \pm 0.08$, as opposed to $R_\mathrm{d}/R_\mathrm{PSF} = 0.61 \pm 0.02$ for all KROSS galaxies. We caution that in this situation it is more difficult to recover the intrinsic velocity dispersion. Galaxies that lie *above* the model trends tend to be those where the dispersion comes from the median of all available pixels. As discussed in Section 3.5, these measurements are associated with larger uncertainties. Nevertheless, the median properties of the KROSS sample follow trends similar to those predicted by both models.

Over the SFR range measured by our observations, each model appears to provide an adequate description of the data. For example, adopting a single track for models, with $Q = 1.0$ in the feedback-driven model and $f_\mathrm{g} = 0.5$ in the gravity-driven model, the reduced χ^2 (accounting for measurement errors) agree within $\Delta\chi^2 = 1$ (the individual reduced χ^2 are 3.4 and 4.1 for the gravity-driven and feedback-driven models, respectively). Although some of the scatter will be due to measurement errors, there will be intrinsic variations within the sample in Q_g and f_g and we will investigate this further in the next section.

5.3.2 Best-fitting model Toomre Q and gas fractions

Directly comparing the observed velocity dispersions to those predicted by the analytical models is not an efficient test of gravity-driven turbulence versus feedback-driven turbulence. Offsets for the

[3] We adopt the same fiducial values of $\epsilon_\mathrm{ff} = 0.01$, $\phi_\mathrm{P} = 3$, $r_1 = 10$, $r_0 = 0.1$, $\phi = 1$, $\mathcal{F} = 2$, and $p_\star/m_\star = 3000$

Downloaded from https://academic.oup.com/mnras/article-abstract/474/4/5076/4655192 by University of Queensland Library user on 07 February 2020

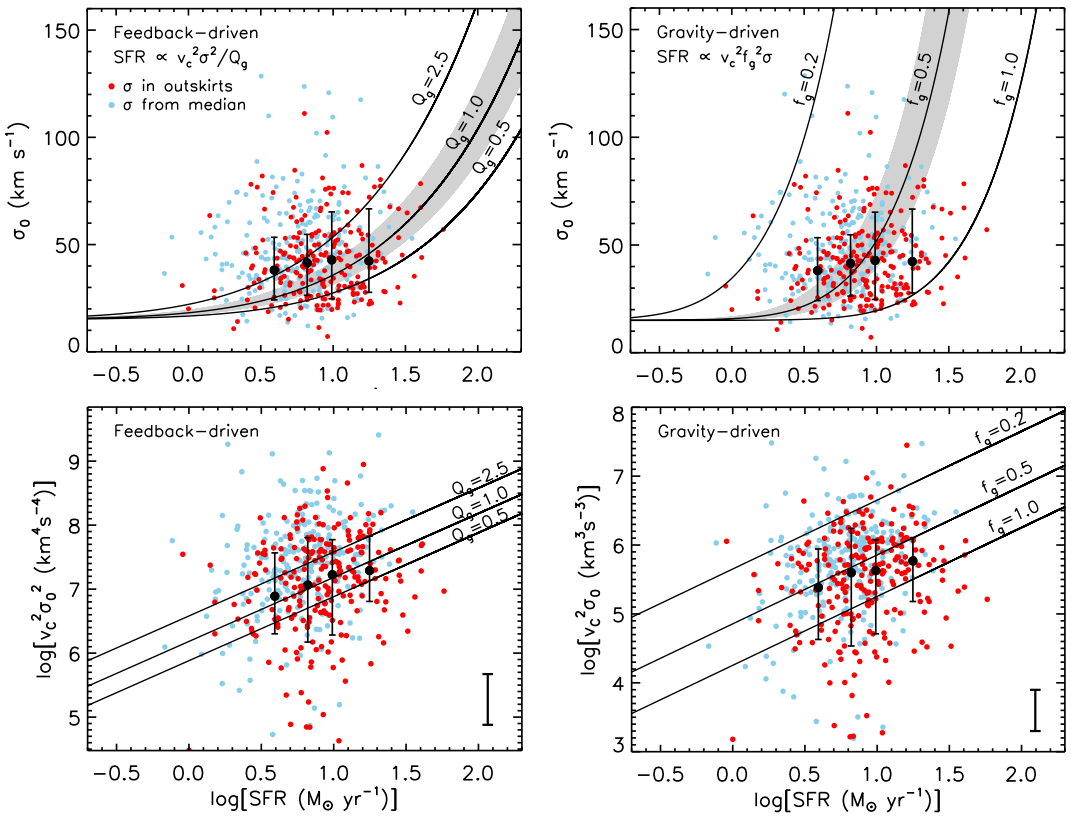

Figure 11. Properties of KROSS galaxies compared to predictions of the analytic models discussed in Section 5. Points are coloured by the technique used to measure the velocity dispersion, σ_0. Large black symbols show the median dispersion (and standard deviation) in bins of SFR. Top left: Predictions of a model in which turbulence is driven by star formation feedback (see Section 5.2, equation 9) assuming the median rotation velocity of the sample ($v_C \approx 120\,\mathrm{km\,s^{-1}}$) and a gas Toomre parameter of $Q_g = 0.5$, 1.0, 2.0. The shaded region shows the impact of increasing/decreasing the rotation velocity by $20\,\mathrm{km\,s^{-1}}$; the 68th percentile range of our data is $v_C = 44$–$204\,\mathrm{km\,s^{-1}}$ so we would expect a large amount of scatter even if only one value of Q_g was valid. Top right: Predictions of a model in which turbulence is driven by gravitational instabilities (see Section 5.1, equation 7), assuming the median v_C and gas fractions of $f_g = 0.25$, 0.5, 1.0. This model results in a much steeper increase in σ_0 as a function of SFR. We measure $\sigma_0 \geq 100\,\mathrm{km\,s^{-1}}$ for only a handful of KROSS galaxies, and do not observe a strong trend with SFR. However this model could still be valid if the galaxies have a wide range of rotation velocities and/or gas fractions. Bottom: To eliminate dependency on the rotation velocity, we also plot $\log(v_C^2\sigma_0^2)$ and $\log(v_C\sigma_0^2)$ as a function of SFR for the feedback- and gravity-driven models, respectively (in both panels, we plot a representative error bar to highlight the uncertainty on individual measurements). Both models provide an adequate description of the data, however there is a large amount of residual scatter. This could be due to measurement uncertainties, an intrinsic variation of Q_g and f_g, or (most likely) a combination of these two factors.

feedback-driven model tend to be smaller than for the gravity-driven model, since the latter has a much steeper relationship between SFR and velocity dispersion. An alternative approach is to calculate the Toomre parameter and gas fraction required for each galaxy to be fit by the models. These are properties which we can also estimate directly from the observations, independent of any turbulence model, with a few simple assumptions. By comparing these two sets of parameters, we can test which model provides a better fit to the data.

In Fig. 12, we compare the distribution of Toomre Q_g values inferred from the feedback-driven turbulence model (rearranging equation 9) to those estimated using equation (8). To estimate the gas surface density we calculate the SFR surface density and then invert the Kennicutt–Schmidt relation, $\Sigma_{SFR} = A\,\Sigma_{gas}^n$, where $A = 1.5 \times 10^{-4}\,\mathrm{M_\odot\,yr^{-1}\,pc^{-2}}$ and $n = 1.4$ (Kennicutt 1998; for a Chabrier IMF). We note that an alternative approach would be to estimate Σ_{gas} by inverting the multi-freefall star formation relation (Federrath et al. 2017b); however, this is not something we explore here. We find a median of $Q_{g,\,med} = 1.6 \pm 0.2$ for the model and $Q_{g,\,med} = 1.01 \pm 0.06$ for the empirically derived values (close to the $Q_g \sim 1$ expected for a marginally unstable disc). The model distribution is noticeably broader, with a 68th percentile range of 7.0 as opposed to 2.1 for the empirically derived values.

In Fig. 12, we also compare gas fractions inferred from the gravity-driven turbulence model (rearranging equation 7) to those calculated using the inverse Kennicutt–Schmidt relation. We estimate the gas mass within twice the half-light radius, and then express this as a fraction of the total baryonic mass $f_g = M_g/(M_g + M_\star)$. We find a median of $f_{g,med} = 0.52 \pm 0.02$ for the model and $f_{g,med} = 0.45 \pm 0.01$ for the empirically derived values. In comparison, the relations described in Section 4.4 predict an average gas fraction of $f_g = 0.41 \pm 0.02$. The model distribution is again the broadest, with a 68th percentile range of 0.95 compared to 0.44 for the observations, and this additional scatter results in unphysical values of $f_g > 1$ for ∼25 per cent of galaxies.

Thus, over the mass and redshift range probed by our observations, both models can provide a reasonable match to the observations and as such, we are unable to definitively rule out either turbulence mechanism at this mass and SFR. First, we note that the medians of the distributions for model and empirically derived

Downloaded from https://academic.oup.com/mnras/article-abstract/474/4/5076/4655192 by University of Queensland Library user on 07 February 2020

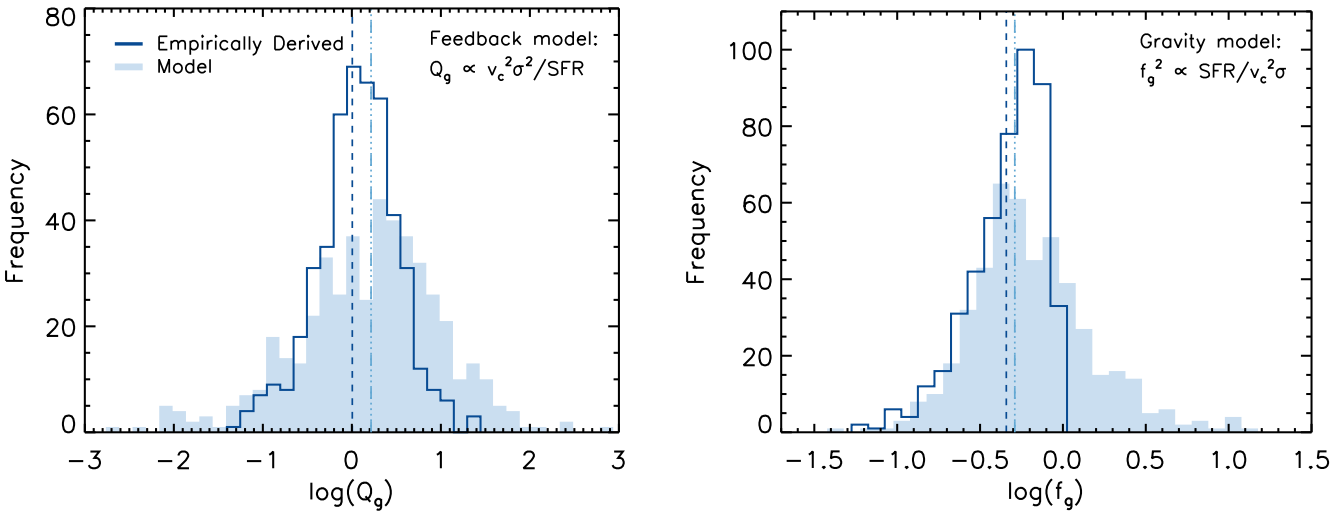

Figure 12. Toomre parameters and gas fractions required for the turbulence models in Section 5 to fit KROSS galaxies, compared to estimates of these properties made from observations. Dashed vertical lines show the median of each distribution. Left: Model (equation 9, filled histogram) versus empirically derived (outlined histogram) Toomre Q_g. The model distribution is broader and has a slightly larger median – $Q_{g,med} = 1.6 \pm 0.2$ as opposed to $Q_{g,med} = 1.01 \pm 0.06$. Right: Model (equation 7, filled histogram) versus empirically derived (outlined histogram) gas fractions. Model values have a similar median – $f_{g,med} = 0.52 \pm 0.02$ versus $f_{g,med} = 0.45 \pm 0.01$. In both panels, the offset between distributions is small and could be accounted for with a minor adjustment in model parameters. We are unable to definitively rule out either turbulence model. Uncertainties associated with the best-fitting model parameters are approximately twice as large, which may explain why these distributions are broader.

quantities are very similar. For the gravity-driven model, increasing the SFR per freefall time from $\epsilon_{ff} = 0.01$ to 0.013 in equation (7) would eliminate the offset completely [note Federrath (2013, 2015) suggests values between $\epsilon_{ff} = 0.01$ and 0.02]. For the feedback-driven model, this could be achieved by adjusting $\mathcal{F} = 2$ to $\mathcal{F} = 3$ in equation (9). This dimensionless normalization parameter ensures that the model fits observations of the relationship between gas surface density and SFR surface density (fig. 4 of Faucher-Giguère et al. 2013). Such an increase would be inconsequential in this regard.

Secondly, although the distributions of the best-fitting model parameters are much broader and include unphysical or implausible values (e.g. $f_g > 1$ or $Q_g > 100$), this is likely due to measurement uncertainties. Estimates of the Toomre Q_g parameter for the model have a stronger dependence on rotation velocity and velocity dispersion than the observational estimates. Similarly, best-fitting model gas fractions depend on v_C and σ but the observational estimates do not. These dynamical parameters are the largest source of uncertainty and as such, fractional errors associated with model Q_g and f_g values are approximately twice as large as for the empirically derived values.

Direct observation of the molecular gas component would help to provide further constraints. If turbulence in the ISM is gravity driven, we would expect the velocity dispersion to be strongly dependent on the gas fraction ($\sigma \propto 1/f_g^2$). However, in a feedback-driven scenario, the two properties should not be related.

We note that these conclusions do not contradict the previous analysis by Krumholz & Burkhart (2016) who concluded that the better match to observations is from the gravity-driven turbulence model. Their conclusion is mainly driven by the match to the galaxies with the highest SFRs, for which we have few galaxies in our sample. However, it is interesting to also note that Krumholz et al. (2017) predict a transition from mostly gravity-driven turbulence at high redshift to feedback-driven turbulence at low redshift. They argue that this evolution would explain why bulges form at high redshift and discs form at lower redshift. Galaxies at $z \sim 0.9$ (of a similar mass to the KROSS sample) would be expected to have a ratio between star formation-supported dispersion (σ_{SF}) and total gas velocity dispersion (σ_g) of $\sigma_{SF}/\sigma_g \sim 0.3$–0.4. In this context, it would be unsurprising that we are unable to definitively rule out either model.

6 CONCLUSIONS

In this work, we have analysed the velocity dispersion properties of 472 Hα-detected star-forming galaxies observed as part of KROSS (Stott et al. 2016; Harrison et al. 2017). KROSS is the largest near-infrared IFU survey of $z \sim 1$ galaxies to date, and consists of a mass- and colour-selected sample that is typical of the star-forming 'main sequence' at this redshift. Mitigating the effects of beam smearing is essential to understanding the dynamics of high-redshift galaxies, and in Appendix B, we present a detailed analysis of this phenomenon. We derive correction factors as a function of R_d/R_{PSF} (the ratio between the galaxy radius and half of the spatial PSF) that we apply to our measurements of rotation velocity and velocity dispersion. Our key results are as follows:

(i) Galaxies at this epoch are highly turbulent with large intrinsic velocity dispersions. We measure a median dispersion of $\sigma_0 = 43.2 \pm 0.8\,\mathrm{km\,s^{-1}}$ and rotational velocity to dispersion ratio of $v_C/\sigma_0 = 2.6 \pm 0.1$ for galaxies with stellar masses of $\log(M_\star/M_\odot) = 8.7$–11.0. Although dynamically hotter than their local counterparts, the majority of our samples are rotationally dominated (83 ± 5 per cent). We observe a strong increase in v_C/σ_0 with increasing stellar mass: evidence of 'kinematic downsizing'.

(ii) We combine KROSS with data from SAMI ($z \sim 0.05$; Croom et al. 2012) and an intermediate-redshift MUSE survey ($z \sim 0.5$; Swinbank et al. 2017) to explore the relationship between intrinsic

Downloaded from https://academic.oup.com/mnras/article-abstract/474/4/5076/4655192 by University of Queensland Library user on 07 February 2020

velocity dispersion, stellar mass, and SFR. At a given redshift, we see, at most, a $\sim$15 km s^{-1} increase in dispersion for a factor of $\sim$100 increase in stellar mass.

(iii) All three samples (SAMI, MUSE, and KROSS) are consistent with a weak increase in velocity dispersion with increasing SFR. We see an increase of 20–25 km s^{-1} across three orders of magnitude in SFR. This trend appears to be independent of redshift.

(iv) At a given redshift, the average velocity dispersion is consistent across several orders of magnitude in specific SFR. Normalizing for the effects of SFR and stellar mass, we see a $\sim$50 per cent increase in velocity dispersion between $z \sim 0$ and 0.9.

(v) To understand the dynamics of KROSS in a wider evolutionary context, we consider five additional samples between $0 < z < 2.5$. We find an increase in the average velocity dispersion with redshift, from $\sigma_0 \sim 25$ km s^{-1} at $z = 0$ to $\sigma_0 \sim 50$ km s^{-1} at $z = 2$. After normalizing for the effects of stellar mass, we also find a decrease in the average v_C/σ_0 ratio for a $\log(M_\star/M_\odot) = 10.5$ galaxy, from $v_C/\sigma_0 \sim 6$ at $z = 0$ to $v_C/\sigma_0 \sim 2$ at $z = 2$.

(vi) We show that the observed evolution in galaxy dynamics can be reasonably well described by a simple 'toy model', in which galaxies are assumed to be thin discs of constant rotational velocity with higher gas fractions at early times. To provide the best possible fit to the data, this model would require lower redshift samples to be associated with higher average values of Toomre Q_g (a more stable gas disc).

(vii) Finally, we test the predictions of two different analytical models – one which assumes turbulence is driven by stellar feedback and another that assumes it is driven by gravitational instabilities. Each predicts a different relationship between SFR and velocity dispersion, with tracks parametrized by Toomre Q_g or gas fraction, respectively. We find that both models provide an adequate description of the data, with best-fitting parameters close to what we derive independently from the observations, using a different set of assumptions. Direct measurement of the gas fraction, f_g, would help to provide further constraints.

ACKNOWLEDGEMENTS

We thank the anonymous referee for their comments and suggestions, which improved the content and clarity of the paper. This work is based on observations obtained at the Very Large Telescope of the European Southern Observatory. Programme IDs: 60.A-9460; 092.B-0538; 093.B-0106; 094.B-0061; 095.B-0035. HLJ, AMS, CMH, RGB, IRS, and RMS gratefully acknowledge support from the Science and Technology Facilities Council (grant codes ST/K501979 and ST/L00075X/1). AMS acknowledges the Leverhulme Foundation. JPS acknowledges support from a Hintze Research Fellowship. IRS acknowledges support from an ERC Advanced Investigator programme DUSTYGAL 321334 and a Royal Society Wolfson Merit Award. AJB gratefully acknowledges the hospitality of the Australian National University. DS acknowledges financial support from the Netherlands Organisation for Scientific research (NWO) through a Veni fellowship and Lancaster University through an Early Career Internal Grant (A100679). GEM acknowledges support from the ERC Consolidator Grant funding scheme (project ConTExt, grant number 648179) and a research grant (13160) from Villum Fonden. This work is based on observations taken by the CANDELS Multi-Cycle Treasury Program with the NASA/ESA *HST*, which is operated by the Association of Universities for Research in Astronomy, Inc., under NASA contract NAS5-26555. *HST* data were also obtained from the data archive at Space Telescope Science Institute. We thank Holly Elbert, Tim Green, and Laura Pritchard for carrying out some of the KMOS observations and the staff at Paranal.

Finally, we would like to thank the SAMI team for sharing their data with us and Ivy Wong for useful discussion. BC acknowledges support from the Australian Research Council's Future Fellowship (FT120100660) funding scheme. CF gratefully acknowledges funding provided by the Australian Research Council's Discovery Projects (grant numbers DP150104329 and DP170100603). MSO acknowledges the funding support from the Australian Research Council through a Future Fellowship (FT140100255). The SAMI Galaxy Survey is based on observations made at the Anglo-Australian Telescope. The SAMI spectrograph was developed jointly by the University of Sydney and the Australian Astronomical Observatory. The SAMI input catalogue is based on data taken from the Sloan Digital Sky Survey, the GAMA Survey, and the VST ATLAS Survey. The SAMI Galaxy Survey is funded by the Australian Research Council Centre of Excellence for All-sky Astrophysics (CAASTRO), through project number CE110001020, and other participating institutions. The SAMI Galaxy Survey website is http://sami-survey.org/.

REFERENCES

Allen J. T. et al., 2015, MNRAS, 446, 1567
Aumer M., Burkert A., Johansson P. H., Genzel R., 2010, ApJ, 719, 1230
Bacon R. et al., 2010, in Proc. SPIE Conf. Ser. Vol. 7735, Ground-based and Airborne Instrumentation for Astronomy III. SPIE, Bellingham, p. 773508
Bassett R. et al., 2014, MNRAS, 442, 3206
Bland-Hawthorn J. et al., 2011, Optics Express, 19, 2649
Bolzonella M., Miralles J.-M., Pelló R., 2000, A&A, 363, 476
Bournaud F., Elmegreen B. G., Teyssier R., Block D. L., Puerari I., 2010, MNRAS, 409, 1088
Bournaud F. et al., 2014, ApJ, 780, 57
Bruzual G., Charlot S., 2003, MNRAS, 344, 1000
Bryant J. J., Bland-Hawthorn J., Fogarty L. M. R., Lawrence J. S., Croom S. M., 2014, MNRAS, 438, 869
Bryant J. J. et al., 2015, MNRAS, 447, 2857
Burgarella D. et al., 2013, A&A, 554, A70
Burkert A., 1995, ApJ, 447, L25
Burkert A. et al., 2016, ApJ, 826, 214
Calzetti D., Armus L., Bohlin R. C., Kinney A. L., Koornneef J., Storchi-Bergmann T., 2000, ApJ, 533, 682
Catinella B., Giovanelli R., Haynes M. P., 2006, ApJ, 640, 751
Ceverino D., Dekel A., Bournaud F., 2010, MNRAS, 404, 2151
Chabrier G., 2003, PASP, 115, 763
Cortese L. et al., 2014, ApJ, 795, L37
Crain R. A. et al., 2015, MNRAS, 450, 1937
Cresci G. et al., 2009, ApJ, 697, 115
Croom S. M. et al., 2012, MNRAS, 421, 872
Daddi E. et al., 2010, ApJ, 713, 686
Danovich M., Dekel A., Hahn O., Ceverino D., Primack J., 2015, MNRAS, 449, 2087
Davé R., Finlator K., Oppenheimer B. D., 2012, MNRAS, 421, 98
Davies R. et al., 2011, ApJ, 741, 69
Dekel A., Sari R., Ceverino D., 2009, ApJ, 703, 785
Di Teodoro E. M., Fraternali F., Miller S. H., 2016, A&A, 594, A77
Elbaz D. et al., 2011, A&A, 533, A119
Elmegreen B. G., Burkert A., 2010, ApJ, 712, 294
Epinat B. et al., 2008, MNRAS, 388, 500
Epinat B., Amram P., Balkowski C., Marcelin M., 2010, MNRAS, 401, 2113
Epinat B. et al., 2012, A&A, 539, A92

Downloaded from https://academic.oup.com/mnras/article-abstract/474/4/5076/4655192 by University of Queensland Library user on 07 February 2020

Faucher-Giguère C.-A., Quataert E., Hopkins P. F., 2013, MNRAS, 433, 1970
Federrath C., 2013, MNRAS, 436, 3167
Federrath C., 2015, MNRAS, 450, 4035
Federrath C. et al., 2017a, in Crocker R. M., Longmore S. N., Bicknell G. V., eds, Proc. IAU Symp. 322, The Multi-Messenger Astrophysics of the Galactic Centre. Cambridge Univ. Press, Cambridge, p. 123
Federrath C. et al., 2017b, MNRAS, 468, 3965
Förster Schreiber N. M. et al., 2006, ApJ, 645, 1062
Förster Schreiber N. M. et al., 2009, ApJ, 706, 1364
Freeman K. C., 1970, ApJ, 160, 811
Genzel R. et al., 2006, Nature, 442, 786
Genzel R. et al., 2008, ApJ, 687, 59
Genzel R. et al., 2011, ApJ, 733, 101
Genzel R. et al., 2013, ApJ, 773, 68
Genzel R. et al., 2014, ApJ, 785, 75
Genzel R. et al., 2015, ApJ, 800, 20
Glazebrook K., 2013, PASA, 30, 56
Gnerucci A. et al., 2011, A&A, 528, A88
Goldbaum N. J., Krumholz M. R., Forbes J. C., 2015, ApJ, 814, 131
Goldbaum N. J., Krumholz M. R., Forbes J. C., 2016, ApJ, 827, 28
Green A. W. et al., 2010, Nature, 467, 684
Green A. W. et al., 2014, MNRAS, 437, 1070
Green A. W. et al., 2017, preprint (arXiv:1707.08402)
Harrison C. M. et al., 2016, MNRAS, 456, 1195
Harrison C. M. et al., 2017, MNRAS, 467, 1965
Hopkins P. F., Quataert E., Murray N., 2011, MNRAS, 417, 950
Hopkins P. F., Kereš D., Murray N., 2013, MNRAS, 432, 2639
Hopkins P. F., Kereš D., Oñorbe J., Faucher-Giguère C.-A., Quataert E., Murray N., Bullock J. S., 2014, MNRAS, 445, 581
Jones T. A., Swinbank A. M., Ellis R. S., Richard J., Stark D. P., 2010, MNRAS, 404, 1247
Joung M. R., Mac Low M.-M., Bryan G. L., 2009, ApJ, 704, 137
Karim A. et al., 2011, ApJ, 730, 61
Kassin S. A. et al., 2007, ApJ, 660, L35
Kassin S. A. et al., 2012, ApJ, 758, 106
Kennicutt R. C., Jr, 1998, ApJ, 498, 541
Kewley L. J., Dopita M. A., Leitherer C., Davé R., Yuan T., Allen M., Groves B., Sutherland R., 2013, ApJ, 774, 100
Kim W.-T., Ostriker E. C., 2007, ApJ, 660, 1232
Kim C.-G., Ostriker E. C., Kim W.-T., 2013, ApJ, 776, 1
Kim C.-G., Ostriker E. C., Kim W.-T., 2014, ApJ, 786, 64
Klessen R. S., Hennebelle P., 2010, A&A, 520, A17
Krumholz M. R., Burkhart B., 2016, MNRAS, 458, 1671
Krumholz M. R., Dekel A., 2010, MNRAS, 406, 112
Krumholz M. R., Dekel A., McKee C. F., 2012, ApJ, 745, 69
Krumholz M. R., Burkhart B., Forbes J. C., Crocker R. M., 2017, MNRAS, preprint (arXiv:1706.00106)
Lagos C. d. P., Theuns T., Stevens A. R. H., Cortese L., Padilla N. D., Davis T. A., Contreras S., Croton D., 2017, MNRAS, 464, 3850
Law D. R., Steidel C. C., Erb D. K., Larkin J. E., Pettini M., Shapley A. E., Wright S. A., 2009, ApJ, 697, 2057
Law D. R., Steidel C. C., Shapley A. E., Nagy S. R., Reddy N. A., Erb D. K., 2012, ApJ, 759, 29
Lawrence A. et al., 2007, MNRAS, 379, 1599
Le Tiran L., Lehnert M. D., van Driel W., Nesvadba N. P. H., Di Matteo P., 2011, A&A, 534, L4
Leethochawalit N., Jones T. A., Ellis R. S., Stark D. P., Richard J., Zitrin A., Auger M., 2016, ApJ, 820, 84
Lehnert M. D., Nesvadba N. P. H., Le Tiran L., Di Matteo P., van Driel W., Douglas L. S., Chemin L., Bournaud F., 2009, ApJ, 699, 1660
Lehnert M. D., Le Tiran L., Nesvadba N. P. H., van Driel W., Boulanger F., Di Matteo P., 2013, A&A, 555, A72
Lemoine-Busserolle M., Bunker A., Lamareille F., Kissler-Patig M., 2010, MNRAS, 401, 1657
Lilly S. J., Le Fevre O., Hammer F., Crampton D., 1996, ApJ, 460, L1
Livermore R. C. et al., 2012, MNRAS, 427, 688
Livermore R. C. et al., 2015, MNRAS, 450, 1812
Mac Low M.-M., 1999, ApJ, 524, 169
Mac Low M.-M., Klessen R. S., Burkert A., Smith M. D., 1998, Physical Review Letters, 80, 2754
Moiseev A. V., Tikhonov A. V., Klypin A., 2015, MNRAS, 449, 3568
Molina J., Ibar E., Swinbank A. M., Sobral D., Best P. N., Smail I., Escala A., Cirasuolo M., 2017, MNRAS, 466, 892
Momcheva I. G. et al., 2016, ApJS, 225, 27
Nelson E. J. et al., 2016, ApJ, 828, 27
Newman S. F. et al., 2013, ApJ, 767, 104
Noeske K. G. et al., 2007, ApJ, 660, L43
Obreschkow D. et al., 2015, ApJ, 815, 97
Osterbrock D. E., Ferland G. J., 2006, Astrophysics of gaseous nebulae and active galactic nuclei, University Science Books, Sausalito, California
Owers M. S. et al., 2017, MNRAS, 468, 1824
Peng Y.-j. et al., 2010, ApJ, 721, 193
Persic M., Salucci P., 1988, MNRAS, 234, 131
Rousselot P., Lidman C., Cuby J.-G., Moreels G., Monnet G., 2000, A&A, 354, 1134
Saintonge A. et al., 2013, ApJ, 778, 2
Salucci P., Burkert A., 2000, ApJ, 537, L9
Schaller M. et al., 2015, MNRAS, 451, 1247
Schaye J. et al., 2015, MNRAS, 446, 521
Sharp R. et al., 2006, in McLean I. S., Iye M., eds, Proc. SPIE Conf. Ser., Vol. 6269, Ground-based and Airborne Instrumentation for Astronomy. SPIE, Bellingham, p. 62690G
Sharp R. et al., 2015, MNRAS, 446, 1551
Sharples R. M. et al., 2004, in Moorwood A. F. M., Iye M., eds, Proc. SPIE Conf. Ser. Vol. 5492, Ground-based Instrumentation for Astronomy. SPIE, Bellingham, p. 1179
Sharples R. et al., 2013, Messenger, 151, 21
Shetty R., Ostriker E. C., 2012, ApJ, 754, 2
Simons R. C. et al., 2016, ApJ, 830, 14
Simons R. C. et al., 2017, ApJ, 843, 46
Sobral D., Smail I., Best P. N., Geach J. E., Matsuda Y., Stott J. P., Cirasuolo M., Kurk J., 2013a, MNRAS, 428, 1128
Sobral D. et al., 2013b, ApJ, 779, 139
Sobral D. et al., 2015, MNRAS, 451, 2303
Speagle J. S., Steinhardt C. L., Capak P. L., Silverman J. D., 2014, ApJS, 214, 15
Stark D. P., Swinbank A. M., Ellis R. S., Dye S., Smail I. R., Richard J., 2008, Nature, 455, 775
Stone J. M., Ostriker E. C., Gammie C. F., 1998, ApJ, 508, L99
Stott J. P. et al., 2014, MNRAS, 443, 2695
Stott J. P. et al., 2016, MNRAS, 457, 1888
Swinbank A. M. et al., 2011, ApJ, 742, 11
Swinbank A. M., Sobral D., Smail I., Geach J. E., Best P. N., McCarthy I. G., Crain R. A., Theuns T., 2012a, MNRAS, 426, 935
Swinbank A. M., Smail I., Sobral D., Theuns T., Best P. N., Geach J. E., 2012b, ApJ, 760, 130
Swinbank A. M. et al., 2017, MNRAS, 467, 3140
Tacconi L. J. et al., 2010, Nature, 463, 781
Tacconi L. J. et al., 2013, ApJ, 768, 74
Taylor E. N. et al., 2011, MNRAS, 418, 1587
Toomre A., 1964, ApJ, 139, 1217
Turner O. J. et al., 2017a, MNRAS, 471, 1280
Turner O. J., Harrison C. M., Cirasuolo M., McLure R. J., Dunlop J., Swinbank A. M., Tiley A. L., 2017b, MNRAS, preprint (arXiv:1711.03604)
van der Kruit P. C., Allen R. J., 1978, ARA&A, 16, 103
van der Wel A. et al., 2014, ApJ, 792, L6
Vergani D. et al., 2012, A&A, 546, A118
Wang B., Silk J., 1994, ApJ, 427, 759
Whitaker K. E. et al., 2014, ApJ, 795, 104
Wisnioski E. et al., 2011, MNRAS, 417, 2601
Wisnioski E., Glazebrook K., Blake C., Poole G. B., Green A. W., Wyder T., Martin C., 2012, MNRAS, 422, 3339
Wisnioski E. et al., 2015, ApJ, 799, 209

Downloaded from https://academic.oup.com/mnras/article-abstract/474/4/5076/4655192 by University of Queensland Library user on 07 February 2020

Wuyts S. et al., 2013, ApJ, 779, 135
Zhou L. et al., 2017, MNRAS, 470, 4573

SUPPORTING INFORMATION

Supplementary data are available at *MNRAS* online.

Table A1. Intrinsic velocity dispersion and related quantities.

Please note: Oxford University Press is not responsible for the content or functionality of any supporting materials supplied by the authors. Any queries (other than missing material) should be directed to the corresponding author for the article.

APPENDIX A: CATALOGUE

With Harrison et al. (2017), we released a catalogue of all 586 Hα-detected galaxies in the KROSS sample. This is available online at http://astro.dur.ac.uk/KROSS. We have updated the catalogue to include all velocity dispersion measurements discussed in this paper. Examples of this additional data are provided in Table A1.

APPENDIX B: BEAM SMEARING ANALYSIS

B1 Motivation

Integral field spectroscopy has allowed us to study the spatially resolved gas dynamics, star formation, and ISM properties of distant galaxies in unprecedented detail. However, as with any other technique it is not immune to systematics; in particular, observations of galaxy dynamics can be biased as a result of ground-based seeing. Each of the 24 deployable IFUs on KMOS has a spatial sampling of 0.2 arcsec; however, the observations are seeing limited, and as such we must consider the impact of the spatial PSF (the seeing) on our measurements.

As the observations are convolved with the PSF, information from each spatial pixel is combined with that of neighbouring regions – a phenomenon known as 'beam smearing'. Effects of this on the observed gas kinematics are twofold. First, the spectrum at each pixel is contaminated by components of slightly higher or lower velocities, acting to broaden spectral features and increase the observed velocity dispersion. Secondly, if the blueshifted components are brighter than the redshifted components (or vice versa) the intrinsic velocity of the pixel will be shifted slightly. Globally,

Table A1. Intrinsic velocity dispersion and related quantities.

Name	RA (J2000)	Dec. (J2000)	z	$\sigma_{0,\,\mathrm{obs}}$ (km s^{-1})	σ_0 (km s^{-1})	Flag	R_d / R_PSF	Q_g
C-HiZ_z1_111	+49:55:07	00:08:27.2	0.8498	79 ± 40	53 ± 27	M	0.8 ± 0.2	$2.5^{+1.8}_{-1.6}$
C-HiZ_z1_112	+49:55:13	00:09:08.0	0.8539	33 ± 13	33 ± 13	O	0.4 ± 0.1	$0.1^{+0.1}_{-0.1}$
C-HiZ_z1_186	+50:08:04	00:09:05.5	0.8445	46 ± 3	45 ± 3	O	0.3 ± 0.1	$0.2^{+0.1}_{-0.1}$
C-HiZ_z1_195	+50:08:40	00:08:58.0	0.8454	22 ± 5	22 ± 5	O	0.5 ± 0.2	$0.5^{+0.3}_{-0.2}$
C-HiZ_z1_215	+50:11:50	00:09:08.7	0.8441	12 ± 3	11 ± 3	O	0.6 ± 0.2	$1.3^{+2.7}_{-0.9}$
C-HiZ_z1_224	+50:13:05	00:08:27.7	1.0137	46 ± 23	40 ± 20	M	0.7 ± 0.2	$0.9^{+0.7}_{-0.6}$
C-HiZ_z1_230	+50:13:39	00:09:02.1	0.8445	48 ± 3	46 ± 3	O	0.2 ± 0.1	$0.6^{+0.3}_{-0.3}$
C-HiZ_z1_231	+50:13:40	00:08:38.6	0.8377	58 ± 2	55 ± 2	O	0.3 ± 0.1	$0.1^{+0.1}_{-0.1}$
C-HiZ_z1_235	+50:14:02	00:08:30.2	0.8378	85 ± 42	37 ± 18	M	0.3 ± 0.1	$0.8^{+0.9}_{-0.6}$
C-HiZ_z1_245	+50:15:26	00:07:27.4	0.8334	66 ± 33	52 ± 26	M	1.0 ± 0.3	$1.7^{+1.2}_{-1.1}$
C-HiZ_z1_246	+50:15:33	00:09:17.8	0.8422	51 ± 26	32 ± 16	M	0.5 ± 0.1	$0.8^{+0.6}_{-0.6}$
C-HiZ_z1_251	+50:15:57	00:09:20.7	0.8544	57 ± 10	45 ± 8	O	0.2 ± 0.1	$0.9^{+0.6}_{-0.5}$
C-HiZ_z1_255	+50:16:17	00:09:19.6	0.8502	41 ± 21	34 ± 17	M	0.9 ± 0.3	$1.4^{+1.0}_{-0.9}$
C-HiZ_z1_257	+50:16:24	00:09:05.6	0.8501	73 ± 14	66 ± 13	O	0.3 ± 0.1	$0.9^{+0.6}_{-0.5}$
C-HiZ_z1_258	+50:16:25	00:07:31.8	0.8376	43 ± 21	38 ± 19	M	1.3 ± 0.4	$2.1^{+1.5}_{-1.4}$
C-HiZ_z1_263	+50:17:11	00:08:42.1	0.8370	41 ± 10	40 ± 10	O	0.3 ± 0.1	$0.3^{+0.2}_{-0.2}$
...	...	...	...	...	...	...	...	...

Notes. A catalogue of all 586 Hα-detected galaxies in the KROSS sample is available online at http://astro.dur.ac.uk/KROSS. Columns $\sigma_{0,\,\mathrm{obs}}$ and σ_0 are the observed and beam smearing corrected velocity dispersions, respectively. Corrections were applied as a function of $R_\mathrm{d}/R_\mathrm{PSF}$ – the ratio between the disc radius (in arcsec) and half of the seeing FWHM (see Section 3.6). We flag whether the dispersion was measured in the outskirts of the disc (O), or from the median of all available pixels (M). We also provide the global Toomre Q_g parameter for each galaxy, which we derived by inverting the Kennicutt–Schmidt relation to estimate Σ_gas.

Downloaded from https://academic.oup.com/mnras/article-abstract/474/4/5076/4655192 by University of Queensland Library user on 07 February 2020

this results in the rotation curve appearing flatter than it may be intrinsically.

Understanding the kinematics of our sample is central to achieving the key science goals of KROSS, e.g. investigating the origins of disc turbulence and studying angular momentum. It is therefore essential that we calibrate for the effects of beam smearing. Here, we investigate the systematic effects of beam smearing by creating a series of mock KMOS observations. This will allow us to constrain the biases introduced and derive an efficient method of correcting for them.

B2 Methods

To explore the impact of beam-smearing on our observations, we create a catalogue of $\sim 10^5$ model galaxies, with properties to uniformly sample the KROSS parameter space. For each galaxy, we create two sets of mock IFU observations. First, we model what the ionized gas dynamics would look like in the absence of atmospheric turbulence (i.e. KMOS sampling the intrinsic properties of the galaxy). Secondly, we generate the same dynamical maps for observations made under seeing-limited conditions. Differences between the two data sets will allow us to understand how beam smearing affects measurements of the rotation velocity (v) and intrinsic velocity dispersion (σ_0) and learn how to correct for it.

B2.1 Intrinsic properties of the model galaxies

In the local Universe, galaxy dynamics can be described by the contribution of a rotating disc of gas and stars plus a dark matter halo, with the velocities added in quadrature as $v^2 = v_h^2 + v_d^2$. To create model galaxies, we apply the same principle, making some simple assumptions about each component, following Swinbank et al. (2017). First, we assume that the baryonic surface density follows an exponential profile (Freeman 1970) characterized by a disc mass (M_d) and scale length (R_d):

$$\Sigma_d(r) = \frac{M_d}{2\pi R_d^2} e^{-r/R_d}. \quad \text{(B1)}$$

The contribution of this disc to the circular velocity of the galaxy is

$$v_d^2(x) = \frac{1}{2}\frac{GM_d}{R_d}(3.2x)^2(I_0K_0 - I_1K_1), \quad \text{(B2)}$$

where $x = R/R_d$ and I_n, K_n are the modified Bessel functions computed at $1.6x$. For the halo, we assume $v_h^2 = GM_h(< r)/r$ with a dark matter density profile described by a core radius (r_c) and effective core density (ρ_{dm}):

$$\rho(r) = \frac{\rho_{dm} r_c^3}{(r + r_c)(r^2 + r_c^2)}, \quad \text{(B3)}$$

(Persic & Salucci 1988; Burkert 1995; Salucci & Burkert 2000). This results in a velocity profile of the form

$$v_h^2(r) = \frac{6.4 G \rho_{dm} r_c^3}{r} \times \left\{ \ln\left(1 + \frac{r}{r_c}\right) - \tan^{-1}\left(\frac{r}{r_c}\right) + \frac{1}{2}\ln\left(1 + \left(\frac{r}{r_c}\right)^2\right)\right\}. \quad \text{(B4)}$$

The dark matter fraction of a galaxy (f_{dm}) greatly influences the shape of its rotation curve; hence, it is important that the dark matter properties of our model galaxies closely match those of the KROSS sample. To satisfy this, we exploit results of the 'Evolution and Assembly of GaLaxies and their Environments' cosmological simulation suite (EAGLE; Crain et al. 2015; Schaye et al. 2015). These are a set of hydrodynamical simulations, including subgrid modelling of star formation and stellar feedback, as well as feedback from supermassive black hole accretion. The EAGLE simulations produce galaxies that closely match the observed Universe and so provide an ideal way to estimate f_{dm} for our $z \sim 1$ sample. Considering star-forming galaxies of a similar mass ($10^9 < M_d < 10^{11}$) and redshift ($0.8 < z < 1.0$), we find a median and 1σ range of $f_{dm} = 0.75 \pm 0.10$ within the central 10 kpc (Schaller et al. 2015). From this we can infer suitable values for ρ_{dm}.

To complete our galaxy model, we assume that the intrinsic velocity dispersion of ionized gas (σ_0) is uniform across the disc and that the distribution of Hα (the emission line from which we measure the kinematics) is exponential. Following the results of Nelson et al. (2016), we assume that the Hα emission is more extended than the stellar continuum, with $R_{H\alpha} \sim 1.1\,R_d$. How we define the distribution of light is significant, since beam smearing effects are luminosity weighted. Star-forming galaxies at $z \sim 1$ often appear irregular or 'clumpy' in Hα, and in Section B5.2, we explore how this may impact our results.

From this simple prescription, we create a series of intensity maps, velocity maps, and velocity dispersion maps for model galaxies with similar properties to those in the KROSS sample. We vary the disc mass, disc scale length, inclination, dark matter fraction, and intrinsic velocity dispersion as follows:

(i) $9.0 \leq \log(M_d / M_\odot) \leq 11.2$; steps of 0.15
(ii) $0.5 \leq R_d \leq 2.5$ kpc; steps of 0.25 kpc
(iii) $20 \leq \theta \leq 70$ deg; steps of 5 deg
(iv) $0.65 \leq f_{dm} \leq 0.85$; steps of 0.10
(v) $20 \leq \sigma_0 \leq 80\,\mathrm{km\,s^{-1}}$; steps of $10\,\mathrm{km\,s^{-1}}$

B2.2 Mock IFU observations

After defining the intrinsic properties of a given galaxy, we wish to understand how the same dynamical maps may look under ground-based seeing conditions. To model this, we generate a mock observation of the galaxy, forming a KMOS data cube that we can then convolve with the seeing PSF. Whilst pixel scale of this cube is set to match the spatial resolution of our observations (0.1 arcsec), we choose to retain a high *spectral* resolution ($R \sim 10\,000$) and omit instrument noise. This allows us to attribute any difference between the model and 'observed' data to beam smearing alone. The x–y footprint of the array is initially also larger than the 2.8×2.8 arcsec size of the KMOS IFU, to allow for light outside of this region that may be introduced to the IFU pixels via beam smearing.

At each pixel, we create a spectrum consisting of the Hα emission line and [N II] doublet, assuming that each line is described by a Gaussian profile with a linewidth set by the dispersion and redshift set by the rotation velocity at that position. For simplicity, we adopt a fixed Hα/[N II] ratio and set the flux ratio of the [N II] $\lambda\lambda$6548, 6583 doublet to be 3.06 (Osterbrock & Ferland 2006). To simulate the effects of beam smearing, we then convolve each wavelength slice with the spatial PSF. We model a range of atmospheric conditions, with $\mathrm{FWHM_{seeing}} = 0.5$–$0.9$ arcsec in increments of 0.1 arcsec, and assume a Gaussian profile each time. The median for our KROSS observations is 0.7 arcsec with a standard deviation of 0.17 arcsec, so this range encompasses the data well. Finally, we extract a

Downloaded from https://academic.oup.com/mnras/article-abstract/474/4/5076/4655192 by University of Queensland Library user on 07 February 2020

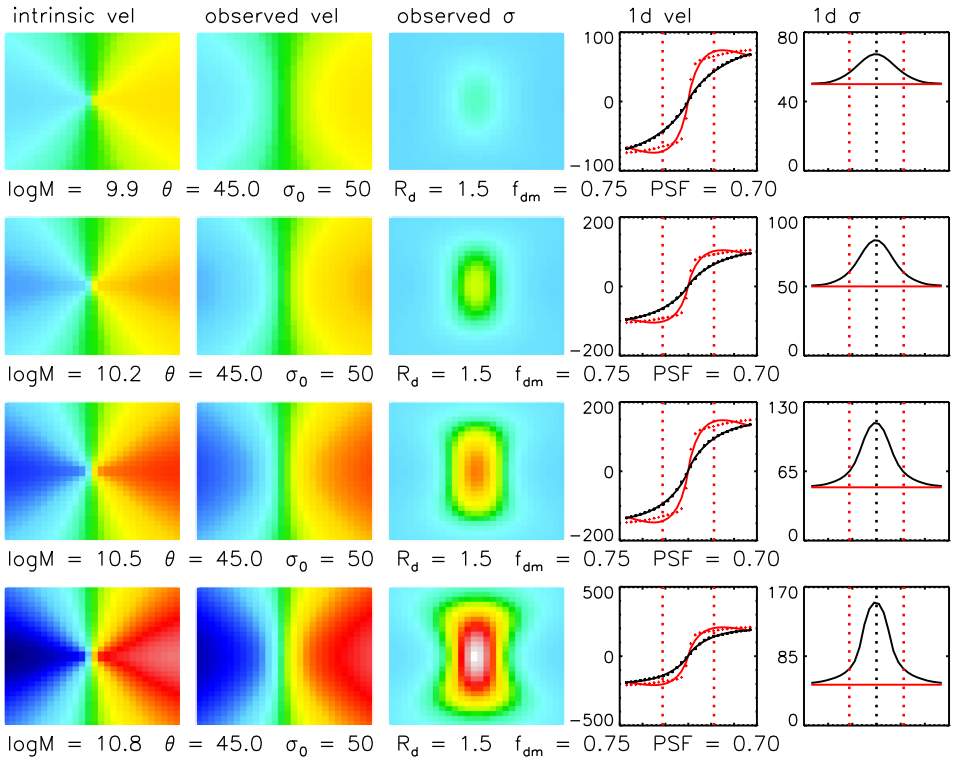

Figure B1. Dynamical maps for a subset of $\sim 10^5$ model galaxies created to explore the impacts of beam smearing. We investigate how closely we can recover the intrinsic velocity and velocity dispersion of a galaxy as a function of disc mass. In successive rows, we increase the mass of the model whilst keeping all other parameters fixed. An increase in mass results in a steeper velocity gradient across the disc. This leads to a stronger beam smearing effect, with a larger peak in the observed velocity dispersion. Left to right: we show the intrinsic velocity map, 'observed' velocity map, and velocity dispersion map, along with the rotation curve and line-of-sight dispersion profile extracted along the primary kinematic axis before (solid red line) and after (black) convolution with the seeing. Dashed red lines represent a radius of $3.4R_{\rm d}$. On each row, we describe the model input parameters where M is disc mass ($M_{\odot}$), θ inclination (deg), σ_0 intrinsic velocity dispersion (km s^{-1}), $R_{\rm d}$ disc radius (kpc), $f_{\rm dm}$ dark matter fraction within 10 kpc, and PSF the full width half-maximum of seeing (arcsec). Each velocity map is scaled between -250 and 250 km s^{-1}, and each dispersion map between 0 and (σ_0+100) km s^{-1}.

subsection of the array to match the size of the KMOS IFU. This is the 'observed' data cube on which we perform our analysis.

To generate dynamical maps from the beam-smeared cube, we fit the emission lines at each pixel using the same χ^2 minimization method as in the data. We require that all lines are Gaussian profiles and share the same linewidth, with the relative positions of the lines and [N II] flux ratio fixed to their model values. These constraints leave the Hα and [N II] intensity, centroid and linewidth free to vary. Since our model does not include noise, spatial binning is not necessary; however, we explore how this process may affect results in Section B5.1. We also extract the rotation curve and one-dimensional dispersion profile of each galaxy. To do so we take the median value of pixels along a 0.7 arcsec 'slit' defined by the major kinematic axis.

B2.3 Kinematic measurements

In order to quantify the effects of beam smearing, we measure the kinematics in the same way as for the KROSS sample (Harrison et al. 2017). Each rotation curve is fit by an exponential disc model of the form

$$v(r)^2 = \frac{r^2 \pi G \mu_0}{R_{\rm d,fit}}(I_0K_0 - I_1K_1) + v_{\rm off}, \quad \text{(B5)}$$

where r is the radial distance, μ_0 is the peak mass surface density, $R_{\rm d,\,fit}$ is the disc radii, $v_{\rm off}$ is the velocity at the kinematic centre, and I_nK_n are Bessel functions evaluated at $\frac{1}{2}\,r/R_{\rm d,\,fit}$. We use this model to interpolate through the data and measure the velocity at a given radius. Other kinematic surveys define the characteristic rotation velocity of a galaxy in various ways. We therefore wish to understand how beam smearing may affect our results as a function of radius. Using the input value of $R_{\rm d}$ for each model, we therefore measure velocities at $2.2R_{\rm d}$, $3.4R_{\rm d}$, and the same again but for radii convolved with the seeing ($R_{\rm d,\,conv}$).

To characterize the velocity dispersion, we record the median of the profile outside $3.4R_{\rm d}$ and also the median of all pixels within the map. Although our simulated galaxies are constructed such that it is possible to make both measurements, for 52 per cent of KROSS galaxies it is only possible to make the latter (due to a large disc scale length or poor S/N). Hence, it is important to understand both parameters. Since beam smearing is expected to be strongest towards the dynamical centre, the median dispersion will likely depend on the maximum radii of detected pixels. We therefore measure the velocity dispersion within both a $2R_{\rm d}$ and $3R_{\rm d}$ aperture.

B3 Results

B3.1 Dynamical maps

Before we perform a more rigorous analysis, quantifying the effects of beam smearing using the variables defined in Section B2.3, we note several trends in the dynamical maps. In Figs B1–B3, we show

Downloaded from https://academic.oup.com/mnras/article-abstract/474/4/5076/4655192 by University of Queensland Library user on 07 February 2020

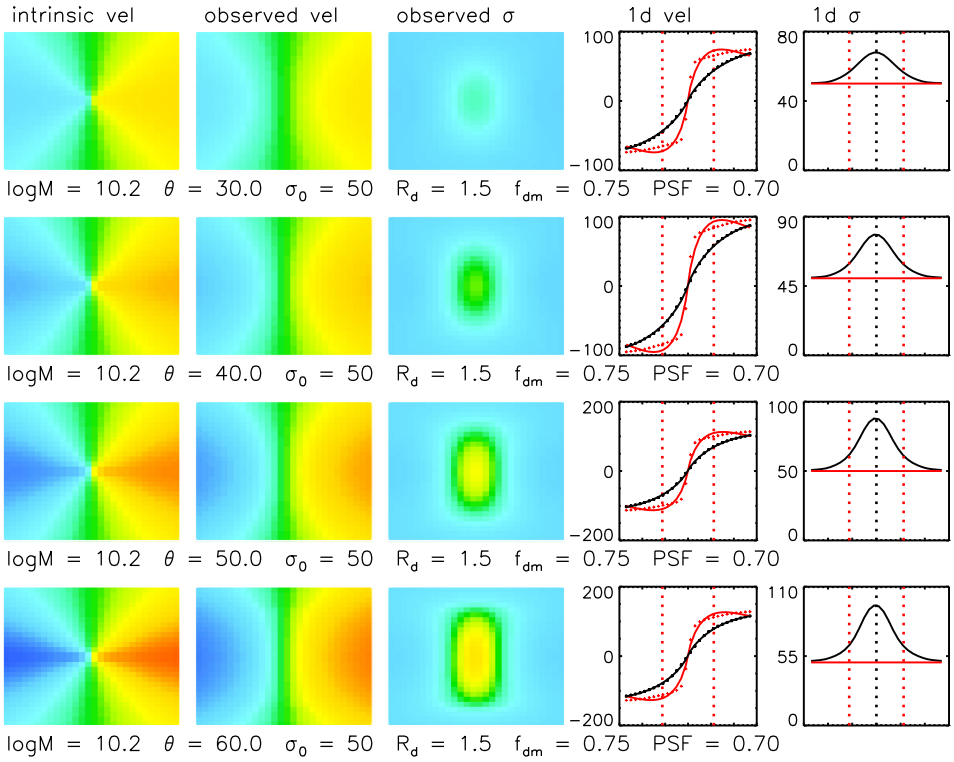

Figure B2. Example dynamical maps and velocity profiles with properties as described in Fig. B1. Left to right: we show the intrinsic velocity map, 'observed' velocity map and velocity dispersion map, rotation curve, and line-of-sight dispersion profile. In successive rows, we increase the inclination of the model whilst all other input parameters remain fixed. As the disc is tilted towards edge-on, the maximum velocity of the rotation curve is increased and contours of the velocity map are pushed closer together (with the characteristic 'spider diagram' shape). A steeper velocity gradient results in a stronger beam smearing effect. The more highly inclined the disc, the larger the peak in the observed velocity dispersion profile.

the dynamical maps, rotation curve, and velocity dispersion profile of 12 model galaxies, where all parameters are kept fixed except for mass (Fig. B1), inclination angle (Fig. B2), or seeing (Fig. B3). We compare the intrinsic kinematics to those recovered after the data cube has been convolved with the spatial PSF. Whilst the extent of the beam smearing depends on the input parameters, the effects are broadly similar in each case. The observed velocity map appears smoother and the observed rotation curve (in black) is flatter than the intrinsic (in red), particularly close to the dynamical centre. The beam-smeared rotation curve also peaks at a lower maximum velocity. Finally, the observed dispersion map is no longer uniform, and we now see a characteristic rise in the region of the steepest velocity gradient.

Fig. B1 explores the relationship between disc mass and beam smearing, and we show four models for which mass is the only parameter allowed to vary. We increase the disc mass over the range $\log(M_{\rm d}\ /\ {\rm M}_{\odot}) = 9.9$–$10.8$ and find that the beam-smearing effect becomes more apparent at each interval. Since the effect of the mass is to increase the steepness of the inner rotation curve, the peak of the observed velocity dispersion profile increases from $\sim$70 km s^{-1} in the low-mass galaxy to $\sim$160 km s^{-1} in the high-mass example. As the disc mass increases, the velocity gradient across the disc becomes larger, hence the components combined by the PSF have a greater velocity difference.

In Fig. B2, we use the same fiducial model as in Fig. B1; however, this time fix the mass as $\log(M_{\rm d}\ /\ {\rm M}_{\odot}) = 10.2$ and vary the inclination from 30 to 60 deg. This figure shows that the more inclined the disc, the greater the beam smearing effect. As the disc approaches edge-on, the iso-velocity contours of the map are 'pinched' together more closely, an effect similar to increasing the disc mass.

Finally, Fig. B3 demonstrates the effect of broadening the spatial PSF. We increase the seeing from 0.6 to 0.9 arcsec and study the impact this has on the observed velocity and velocity dispersion. As with an increase in disc mass or greater disc inclination, poorer atmospheric conditions result in a rotation curve that is shallower than it would be intrinsically. However, whilst the most noticeable effect of increasing the inclination or disc mass is to increase the peak of the dispersion profile, the same is not true of the seeing. An increase in the seeing instead acts to broaden the dispersion profile. At a seeing of 0.6 arcsec the intrinsic dispersion can be recovered at a radius of $\sim 3\,R_{\rm d}$, but for a seeing of 0.9 arcsec the required radius is approximately double.

B3.2 Impact of model parameters

As discussed in Section B3.1, from visual inspection of the dynamical maps it is already possible to identify several trends between model input parameters and the impact of beam smearing. However, we now wish to quantify these effects such that we can apply corrections to our KROSS data.

Galaxies that are small in comparison to the PSF are more affected by beam smearing (Fig. B3), and the shape of the rotation curve and ability to recover σ_0 in the outskirts of the galaxy deteriorate rapidly as the seeing is increased. Since this is perhaps the strongest universal trend, we choose to study how our

Downloaded from https://academic.oup.com/mnras/article-abstract/474/4/5076/4655192 by University of Queensland Library user on 07 February 2020

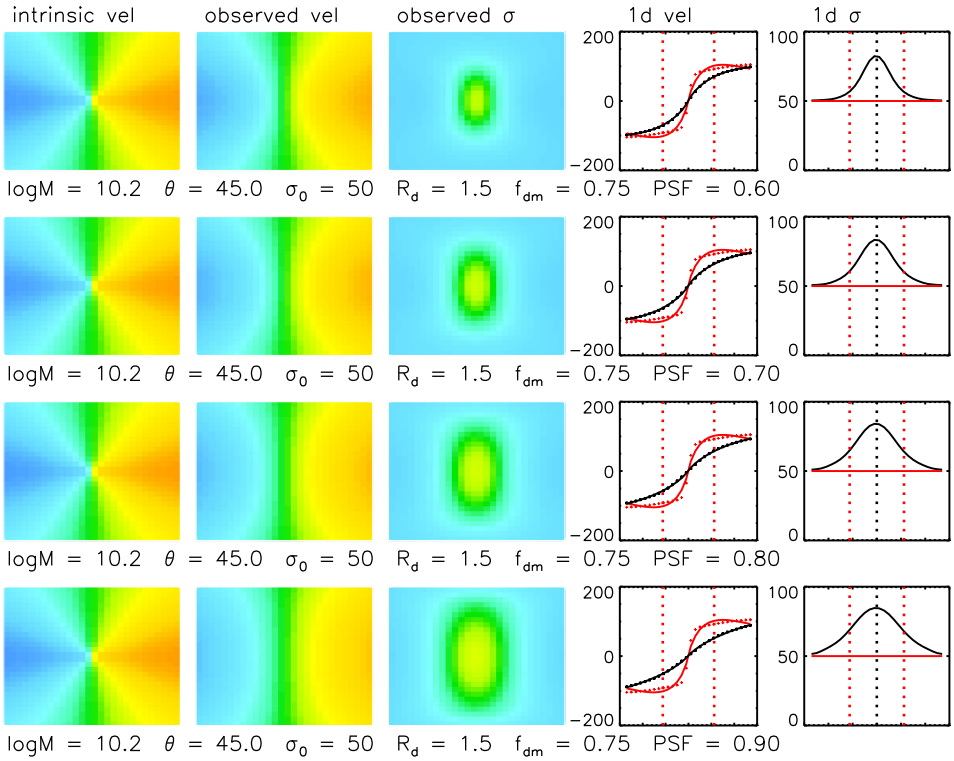

Figure B3. Dynamical maps and velocity profiles with properties as described in Fig. B1. Left to right we show the intrinsic velocity map, 'observed' velocity map and velocity dispersion map, rotation curve and line-of-sight dispersion profile. In successive rows we increase the spatial PSF (the seeing) of the model whilst all other input parameters remain fixed. Poorer atmospheric conditions result in a more severe beam smearing effect. As the seeing is increased, the observed velocity gradient becomes shallower, structure in the velocity map is less visible and the peak in the observed velocity dispersion becomes broader. Whilst at 0.6 arcsec the dispersion measured in the outskirts of the galaxy (beyond $3.4R_{\rm d}$ – red dashed lines) is close to the intrinsic value, at 0.9 arcsec this is a gross overestimate.

measurements of rotation velocity and dispersion are affected as a function of $R_{\rm d}/R_{\rm PSF}$, where $R_{\rm PSF}$ is the half width half-maximum of the spatial PSF. To assess the impact of other variables relative to this, we then bin the data in terms of disc mass (Fig. B4), inclination (Fig. B5), dark matter fraction (Fig. B6), and intrinsic dispersion (Fig. B7) in turn.

In each figure, we demonstrate how four measurements are impacted by beam smearing: the rotation velocity ($v_{\rm out}$) at $3.4R_{\rm d}$, the rotation velocity at the same radius convolved with the seeing, the median of the velocity dispersion profile at radii greater than $3.4R_{\rm d}$ ($\sigma_{\rm out}$), and the median of the velocity dispersion map within a $3R_{\rm d}$ aperture ($\sigma_{\rm out,med}$). Measurements taken at smaller radii result in the same trends but with a systematic offset. We will discuss this further in Section B4.1.

The tracks in Figs B4–B7 confirm many of our conclusions in Section B3.1. That is, for low values of $R_{\rm d}/R_{\rm PSF}$ (i.e. galaxies which are small compared to the spatial PSF), the rotation velocity we recover is an underestimate of the intrinsic value. Nevertheless, as the model galaxy is increased in size (or the seeing is decreased) we approach $v_{\rm out}/v_0 = 1$. When extracting measurements from the rotation curve at $3.4R_{\rm d}$, a ratio of $R_{\rm d}/R_{\rm PSF} = 0.2$ results in an average underestimate of a factor of 2. However, this effect is less significant when we measure at the radius we require convolved with the seeing. Here, the rotation velocity is only underestimated by ∼10 per cent at $R_{\rm d}/R_{\rm PSF} = 0.2$. In Figs B1–B3, we can see why this may be so; outer regions of the galaxy's rotation curve are less affected by beam smearing.

In the lower two panels of Figs B4–B7, we can see that beam smearing affects our ability to recover the intrinsic velocity dispersion even more strongly. The lower the $R_{\rm d}/R_{\rm PSF}$ ratio, the more we overestimate the intrinsic velocity dispersion. Most noticeably, measuring σ in the outskirts of the velocity dispersion profile is a much better estimate than a median of the dynamical map. This is because the beam smearing effects are largest in regions of steep velocity gradients (i.e. towards the dynamical centre of a uniformly rotating disc). We see a range of $\sigma_{\rm out}/\sigma_0 = 1.0$–$1.5$ compared to $\sigma_{\rm out,med}/\sigma_0 = 1.0$–$4.0$ estimated using the map.

Coloured tracks in these figures show the results for models with one particular input parameter fixed and all others allowed to vary. The shaded region illustrates the 1σ range for all 10^5 models. In Fig. B4, we see that higher mass galaxies result in estimates of rotation velocity closer to the intrinsic value, since their rotation curve peaks more quickly, but the systematic offset in σ_0 is larger due to the steeper velocity gradient. The tracks of fixed disc mass cover the 1σ range of the data, suggesting that this is an important parameter.

As discussed in Section B3.1, galaxy models of a higher inclination are more susceptible to beam smearing (Fig. B5). However, the difference between the track for <30 deg and >60 deg inclinations is small, suggesting this effect is secondary to that caused by increasing the disc mass. The same is true for models of varying dark matter fraction (Fig. B6). None the less, it is interesting to note that galaxies with a greater dark matter fraction suffer more beam smearing. We suggest that this is because the dark matter fraction

Downloaded from https://academic.oup.com/mnras/article-abstract/474/4/5076/4655192 by University of Queensland Library user on 07 February 2020

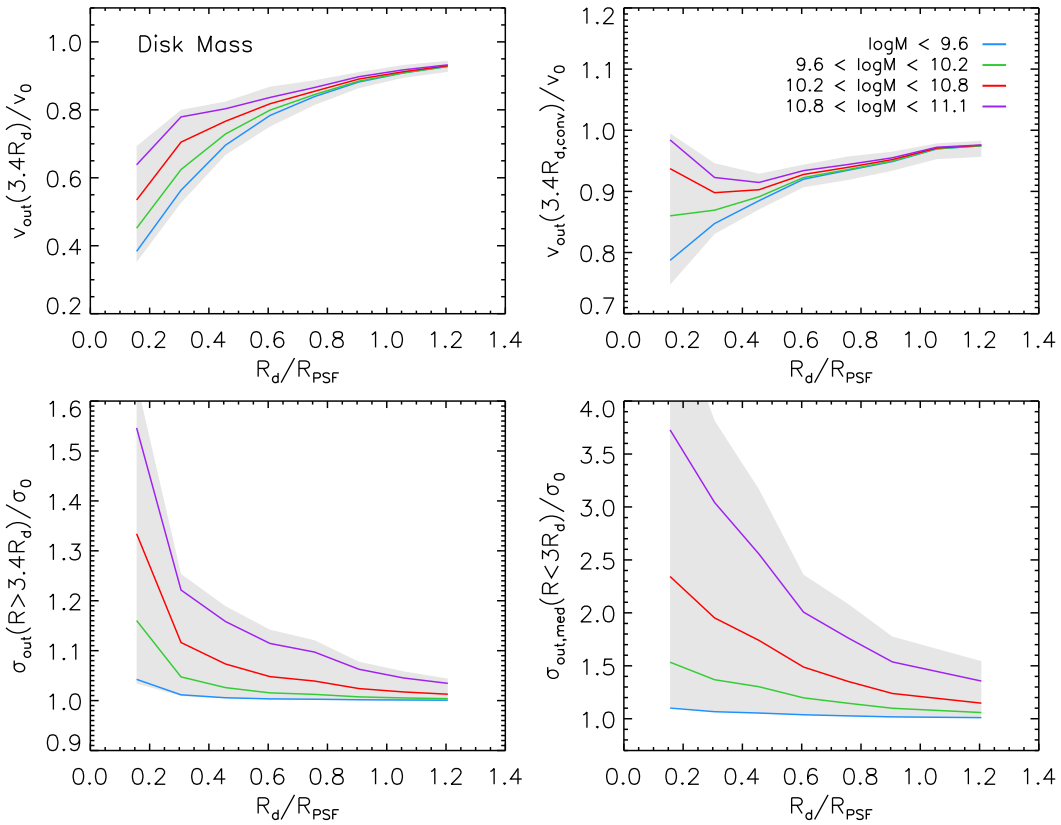

Figure B4. The impact of beam smearing on measurements of rotation velocity and velocity dispersion, as a function of disc mass. R_d/R_{PSF} is the ratio between the disc radius and the half width half-maximum of the PSF, which determines which velocity components are combined by the seeing, and thus the extent of the beam smearing. We split models into four mass bins and plot a running median for each (solid lines). Shaded regions represent the 1σ scatter of all models, showing that disc mass accounts for most, if not all, of this variation. Top left: Model velocity at $3.4R_d$ as a fraction of the intrinsic value (v_0). The lower the R_d/R_{PSF} and the smaller the disc mass, the more we underestimate the true velocity. Top right: Velocity at the same radius convolved with the seeing. This is a better estimate of $v_0(3.4R_d)$, with at most a 20 per cent difference. Bottom left: Median of the velocity dispersion profile beyond $3.4R_d$ as a fraction of the intrinsic (σ_0). The lower the R_d/R_{PSF} and larger the disc mass, the more we overestimate the dispersion, with up to a 50 per cent difference. Bottom right: The median dispersion within an aperture of $3R_d$. This measurement is more susceptible to beam smearing, with overestimates of up to a factor of 4.

determines the degree of turnover in the rotation curve, which in turn affects the velocity gradient across pixels in the outer regions.

Finally, we explore the impact of adjusting the intrinsic velocity dispersion of the model (Fig. 4). We find that the lower the input dispersion, the more successful we are in recovering the true rotation velocity, but that the opposite is true of the velocity dispersion itself. For very low dispersions ($\sigma_0 < 30\,\mathrm{km\,s^{-1}}$), the beam smearing effect is as strong as for very high mass galaxies ($10.8 < \log(M_d/M_\odot) < 11.1$), simply because the ratio of $\Delta\sigma/\sigma_0$ is larger.

B4 Beam smearing corrections

In Section B3.2, we found that adjusting the input parameters our model galaxies can lead to a stronger or weaker beam smearing effect. Now that we understand these systematics, we wish to derive a series of corrections that can be applied to kinematic measurements of the KROSS sample. In this section, we discuss how best this can be achieved.

B4.1 Measurements of rotation velocity

In the top left-hand panels of Figs B4–B7, we plot the relationship between v_{out}/v_0 and R_d/R_{PSF}. The systematic offset between the input and output rotation velocity is strongly correlated with how large the galaxy is compared to the seeing. Values range between $v_{out}/v_0 = 0.5$ and 0.9. However, if we make measurements at the same radii convolved with the seeing (top right-hand panel), this relation is less steep, with a range of only $v_{out}/v_0 = 0.85$–0.95. This is therefore the method we decide to use for the KROSS sample. We note that if we had instead measured the velocity at $2.2R_d$ (a radius commonly used by other kinematic surveys) the results follow a similar trend, with a small shift towards lower v_{out}/v_0, but the effect is $\lesssim$5 per cent.

Whilstvarying model parameters such as disc mass (Fig. B4) and inclination (Fig. B5) introduces scatter in v_{out}/v_0 at the median R_d/R_{PSF} of the KROSS sample ($\sim$0.75), the difference is only a few per cent. Moreover, one of the most dominant influences on the ratio of v_{out}/v_0 is the dark matter fraction, f_{dm}, which we are unable to constrain from our observations. In order to correct the KROSS rotation velocities for beam smearing, we therefore consolidate the information from our models into a single relation for each of $v_{out}(3.4R_d)$ and $v_{out}(2.2R_d)$. We define each correction track as the median outcome of all models, with uncertainties to reflect the 1σ scatter. Data points are fit by an exponential of the form

$$1/\xi_v = v_{out}/v_0 = 1 - Ae^{-B(R_d/R_{PSF})^C}, \quad \text{(B6)}$$

Downloaded from https://academic.oup.com/mnras/article-abstract/474/4/5076/4655192 by University of Queensland Library user on 07 February 2020

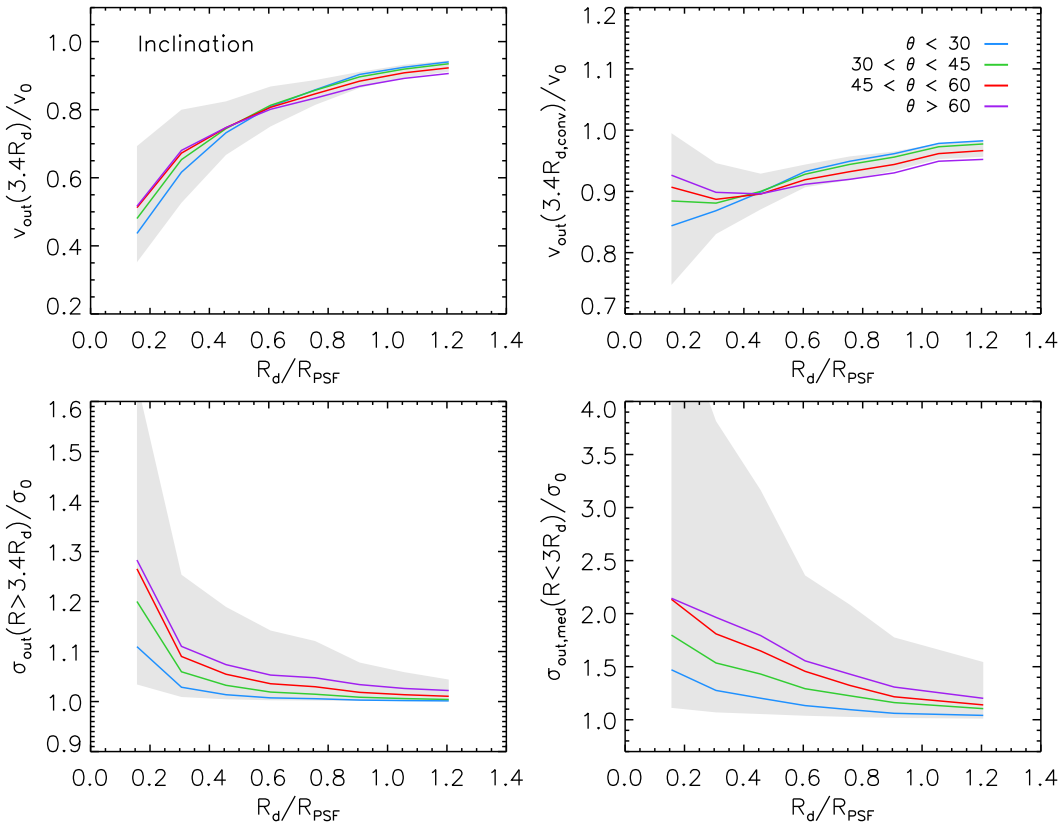

Figure B5. The impact of beam smearing on measurements of rotation velocity and velocity dispersion, as a function of disc inclination. Top left: The lower the R_d/R_{PSF}, the more we underestimate the intrinsic rotation velocity (v_0). The extent of this difference is very similar for models of different inclinations (typically within 5 per cent). Top right: We extract the observed rotation velocity at the required radius convolved with the seeing. This results in a better estimate, but adjusting the inclination appears to have little influence. Bottom left: The lower the R_d/R_{PSF} and the more inclined the disc, the more we overestimate the intrinsic velocity dispersion. The difference between a low inclination model (<30 deg) and a high inclination model (>60 deg) is still relatively minor (∼10 per cent) and cannot account for the full 1σ scatter of the data (shaded region). The trend between disc mass and beam smearing appears to be more dominant. Bottom right: If we estimate the velocity dispersion from a median of the map, as opposed to the outskirts of the dispersion profile, we overestimate σ_0 by almost twice as much.

where A, B, and C are constants defined in Table B1 and ξ_v is the velocity correction factor. We show these final tracks for beam smearing corrections to the rotation velocity in Fig. 3.

B4.2 Measurements of velocity dispersion

The effects of beam smearing on measurements of the intrinsic velocity dispersion (σ_{out}) are generally more significant than for the rotation velocity. In the bottom left-hand and right-hand panels of Figs B4–B7, we see that for galaxies small in comparison to the spatial PSF (i.e. for low R_d/R_{PSF}) the dispersion in the outskirts of the disc can be a factor of ∼1.5 higher than the intrinsic value. Estimates made using the median of the map may even reach $\sigma_{out}/\sigma_0 = 5$. However, for larger galaxies (or a smaller spatial PSF) σ_{out}/σ_0 appears to decrease exponentially.

Binning the data in Figs B4–B7 by disc mass, inclination, dark matter fraction, and intrinsic dispersion reveals that the input parameters of the model have a significant impact on how we measure σ_0. At the median R_d/R_{PSF} of our KROSS sample, the difference between high-mass and low-mass models (for measurements made in the outskirts of the dispersion profile) is $\sigma_{out}/\sigma_0 \sim 0.1$. The difference for discs close to edge-on or face-on is $\sigma_{out}/\sigma_0 \sim 0.05$. Changes to f_{dm} or the input σ_0 itself have less of an impact (unless σ_0 is very small i.e. $< 30\,km\,s^{-1}$), with an average difference of only a few per cent.

Given the strong variation seen in our models, it is clear that we cannot reduce the beam smearing correction to a single track for each of the dispersion measurements (outer disc and median values). Instead, we choose to make corrections as a function of $v_{out}(3.4R_{d,\,conv})$, the rotation velocity measured at a radius of $3.4R_d$ convolved with the seeing (referred to hereafter as v_{out}; not inclination corrected). This combines the effects of the two most dominant parameters: disc mass and inclination. For each method, we split the data into $50\,km\,s^{-1}$ bins of v_{out} and calculate a series of running medians.

Models run with $\sigma_0 < 30\,km\,s^{-1}$ exhibit as much beam smearing as high-mass models; however, we are unable to make corrections as a function of σ_0 (it is what we are trying to measure!). To account for the effect, the intrinsic dispersion has on the beam smearing, we instead resample the model data such that the distribution of σ_{out} matches that of KROSS, and refit the correction tracks.

As discussed in Section B2.3, we measured the median velocity dispersion of each model within two apertures ($2R_d$ and $3R_d$), since the size of the galaxy compared to the IFU, or the surface brightness of the galaxy (hence S/N) will affect the number of available

Downloaded from https://academic.oup.com/mnras/article-abstract/474/4/5076/4655192 by University of Queensland Library user on 07 February 2020

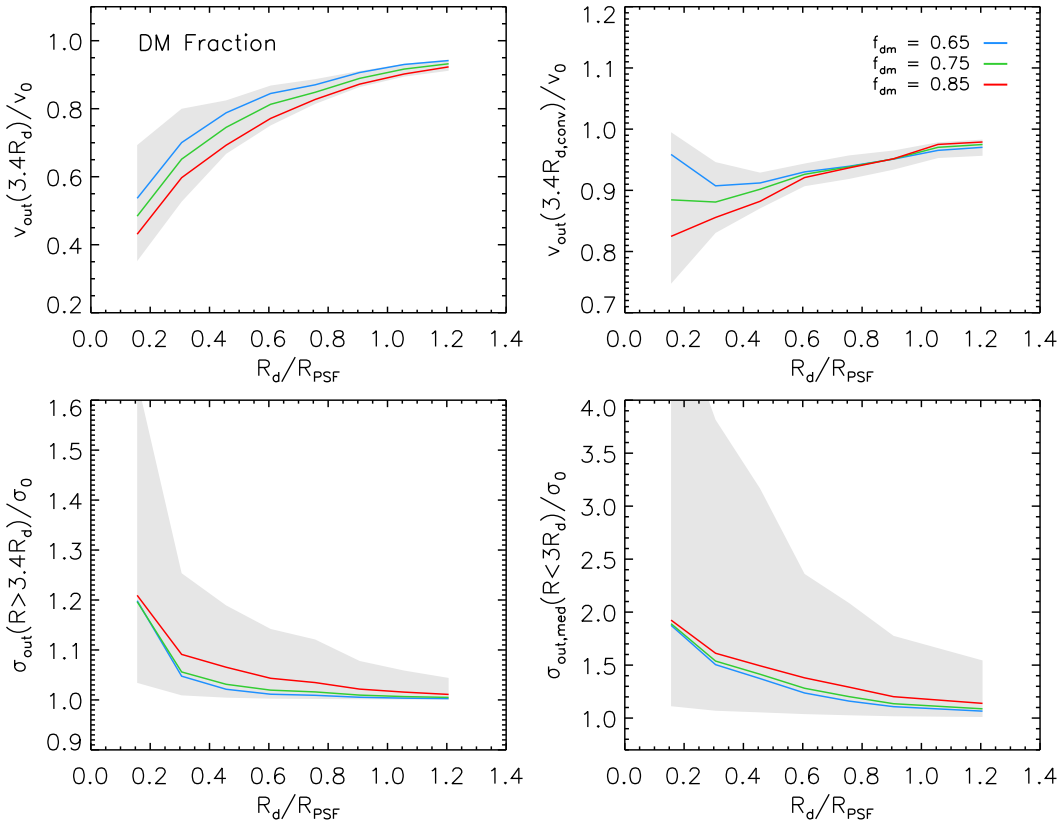

Figure B6. The impact of beam smearing on measurements of rotation velocity and velocity dispersion, as a function of the dark matter fraction within a radius of 10 kpc. Top left: The lower the R_d/R_{PSF} and the larger the dark matter fraction, the more we underestimate the intrinsic rotation velocity (v_0). There is a ∼10 per cent difference between $f_{dm} = 0.65$ and 0.85. Adjusting the dark matter fraction changes the shape of the rotation curve in the outer regions (more or less of a 'turnover'); hence, the velocity components 'merged' by the seeing will be slightly different. Top right: We extract the observed rotation velocity at the required radius convolved with the seeing. This results in a better estimate. For low R_d/R_{PSF}, the difference in f_{dm} models is approximately the same, but for $R_d/R_{PSF} > 0.6$ the models converge. Bottom left: The lower the R_d/R_{PSF}, the more we overestimate the intrinsic velocity dispersion. The difference between models of $f_{dm} = 0.65$ and models of $f_{dm} = 0.85$ is extremely small (a few per cent). Bottom right: If we estimate the velocity dispersion from a median of the map, as opposed to the outskirts of the dispersion profile, we overestimate σ_0 by almost twice as much. Again, the dark matter fraction appears to have little effect on this aspect of beam smearing.

pixels. Fig. B8 compares these two sets of results. If the observed rotation velocity is small ($v_{out} < 100\,km\,s^{-1}$) corrections at the median R_d/R_{PSF} of KROSS range between $\sigma_{out,med}/\sigma_0 = 1.0$ and 1.3 and the difference between results for the two apertures is typically $\sigma_{out,med}/\sigma_0 < 0.1$. If the rotation velocity exceeds this then corrections for the larger and smaller apertures are $\sigma_{out,med}/\sigma_0 = 1.8$ and 2.2, respectively. Since the results are very similar, we therefore combine the results into a single set of (velocity binned) tracks. Final tracks for beam smearing corrections to the velocity dispersion are presented in Fig. 4. The correction σ_{out} to σ_0 as a function of R_d/R_{PSF} is defined by

$$1/\xi_\sigma = \sigma_{out}/\sigma_0 = 1 + Ae^{-B(R_d/R_{PSF})^C}, \quad \text{(B7)}$$

where the constants A, B, and C are defined in Table B1.

B5 Additional tests

B5.1 Adaptive binning

To construct dynamical maps for each of the KROSS galaxies, we employed an 'adaptive binning' technique. In fitting the spectrum of each spaxel (Section B2.2), we required that the Hα emission line was detected with an S/N > 5. If the line was too weak, then we binned the spectra of neighbouring pixels, increasing the size of the region until either the criterion was met, or we reached an area of 0.7×0.7 arcsec (the typical seeing of our observations). To explore how this process may affect measurement of the kinematics, we analyse our model data a second time. When fitting the spectrum of each pixel we now include all data within a 0.5×0.5 arcsec region.

Fig. B9 shows that binning acts to magnify the effects of beam smearing, resulting in lower rotation velocities and greater velocity dispersions. In the instances where data have been binned, the rotation velocity is underestimated by an additional ∼5–10 per cent and the dispersion overestimated by an additional 2–3 per cent (∼5 per cent for large v_{out}). This is a rather exaggerated picture, since in our models have been uniformly binned regardless of the surface brightness profile. In reality, outer regions are more likely to have been binned, and some galaxies may not have been binned at all. Whilst this is an important effect to note, we do not attempt to correct for it, since details of the process are unique to each KROSS galaxy.

Downloaded from https://academic.oup.com/mnras/article-abstract/474/4/5076/4655192 by University of Queensland Library user on 07 February 2020

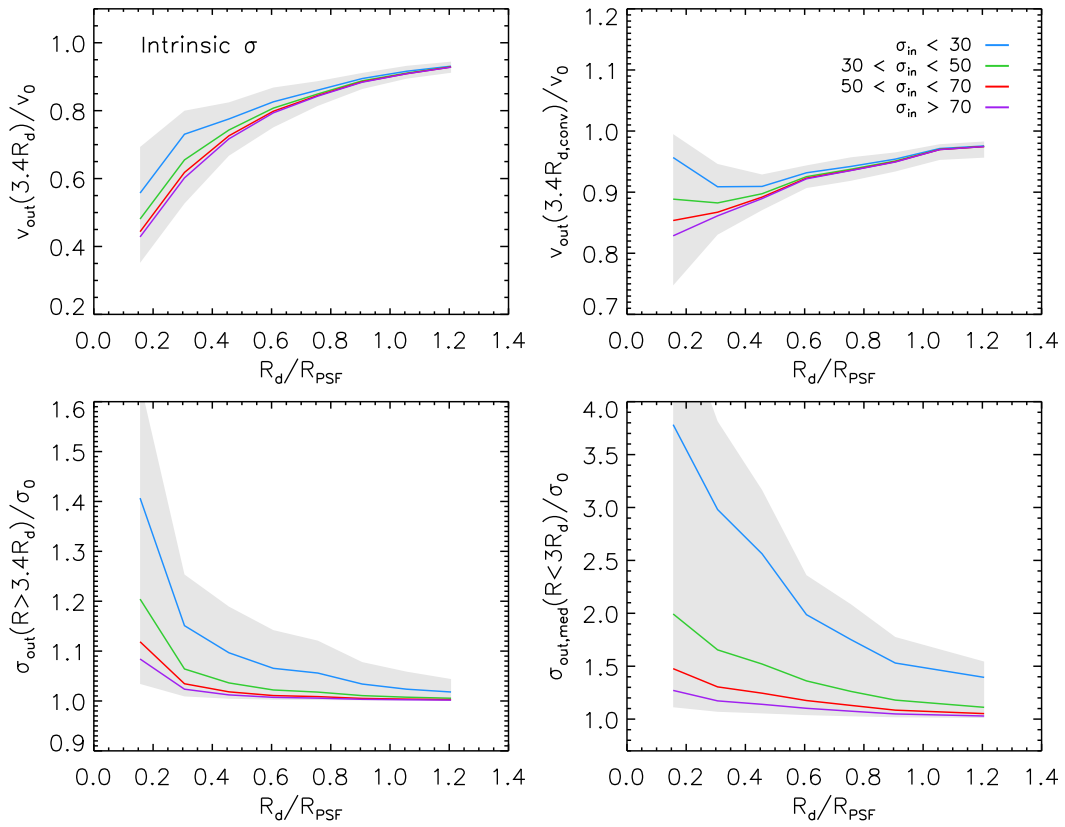

Figure B7. The impact of beam smearing on measurements of rotation velocity and velocity dispersion, as a function of input velocity dispersion. Top left: The lower the R_d/R_{PSF} and the greater the input dispersion of the model, the more we underestimate the intrinsic rotation velocity (v_0). The difference between model galaxies of $\sigma_0 = 30\,km\,s^{-1}$ and $\sigma_0 = 70\,km\,s^{-1}$ is ∼10 per cent at low R_d/R_{PSF}, but the models converge as R_d/R_{PSF} increases. Top Right: We extract the observed rotation velocity at the required radius convolved with the seeing. This results in a better estimate. Again, results for the binned data converge beyond $R_d/R_{PSF} = 0.6$. Bottom left: The lower the R_d/R_{PSF}, the more we overestimate the intrinsic velocity dispersion. The difference between model galaxies of $\sigma_0 = 30\,km\,s^{-1}$ and $\sigma_0 = 70\,km\,s^{-1}$ is as much as ∼30 per cent. How well we can recover the intrinsic velocity dispersion appears to be strongly dependent on what its value was to begin with. Bottom right: If we estimate the velocity dispersion from a median of the map, as opposed to the outskirts of the dispersion profile, it is more difficult to recover σ_0. For very low dispersions ($\sigma_{in} < 30\,km\,s^{-1}$), the beam smearing effect is as strong as for very high-mass galaxies ($10.8 < \log(M/M_\odot) < 11.1$), with σ_0 overestimated by a factor of 4 at low R_d/R_{PSF}.

Table B1. Parametrizationof beam smearing correction tracks.

Correction track	v_{min} ($km\,s^{-1}$)	v_{max} ($km\,s^{-1}$)	A	B	C
Velocity ($3.4R_d$)	–	–	0.18	1.48	1.00
Velocity ($2.2R_d$)	–	–	0.18	1.26	0.88
Dispersion (outskirts)	0	50	0.53	8.22	0.94
	50	100	6.98	7.07	0.52
	100	150	3.27	4.96	0.59
	150	–	2.06	3.67	0.70
Dispersion (median)	0	50	11.50	4.65	0.20
	50	100	52.85	5.55	0.34
	100	150	8.74	3.15	0.77
	150	-	14.15	3.05	0.69

Notes. Constants *A*, *B*, and *C* for the beam smearing correction tracks in Figs 3 and 4, as defined by equations (B6) and (B7). For the velocity dispersion, v_{min} and v_{max} define the range of observed rotation velocities (uncorrected for inclination) that each track covers.

Downloaded from https://academic.oup.com/mnras/article-abstract/474/4/5076/4655192 by University of Queensland Library user on 07 February 2020

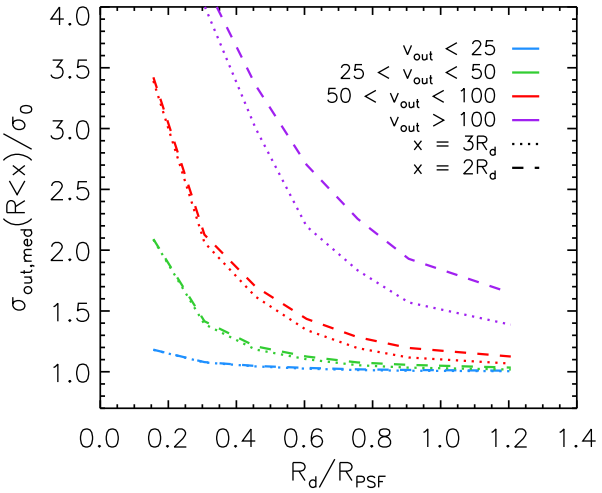

Figure B8. Factor by which the intrinsic velocity dispersion is overestimated when measuring the pixel-by-pixel median within a $3R_d$ (dotted line) or $2R_d$ (dashed line) aperture. If the observed rotation velocity of the galaxy (at $3.4R_{d,\,conv}$) is small, then the two estimates are almost identical (within 10 per cent). For larger velocities ($v_{out} > 100\,km\,s^{-1}$), corrections for the larger and smaller apertures (at the median R_d/R_{PSF} of KROSS) are $\sigma_{out,med}/\sigma_0 = 1.8$ and 2.2, respectively; however, fewer than 25 per cent of our sample satisfy this criterion. We therefore create the final correction tracks (Fig. 4) using only the values for $3R_d$.

B5.2 Intensity maps

For each model galaxy, we have assumed that the stellar mass and light follow an exponential profile, and this was propagated through to the construction of model Hα intensity maps. However, observations suggest that the Hα morphology of $z \sim 1$ galaxies is often irregular, with the presence of ∼kpc scale star-forming 'clumps' (Genzel et al. 2011; Livermore et al. 2012, 2015; Swinbank et al. 2012b; Wisnioski et al. 2012). These deviations from an exponential profile may affect the beam smearing, since within each pixel it will affect the relative contribution of each new velocity component introduced (i.e. beam smearing is luminosity weighted).

In Fig. B10, we compare the results of modelling galaxies with an exponential or a uniform Hα intensity profile. The presence of bright, star-forming clumps may act to flatten the Hα profile, so this is suitable test of how (in the most extreme case) this may affect the beam smearing. Measurements of σ_{out} are less affected by beam smearing in the case of a uniform flux distribution, with a difference of $\sigma_{out}/\sigma_0 \sim 0.1$ on average. Effects on the shape of the rotation curve are also less severe. Pixels in the outskirts of the galaxy are still contaminated by light from central regions; however, these regions are no longer as bright and contribute less flux. Therefore, pixels in the outskirts do not become as skewed towards lower velocities. In the right-hand panel of Fig. B10, we see that the rotation velocity at $3.4R_{d,\,conv}$ is now an overestimate by as much as 20 per cent at low R_d/R_{PSF}. However for $R_d/R_{PSF} > 0.7$, the required corrections are within a few per cent of those for an exponential profile.

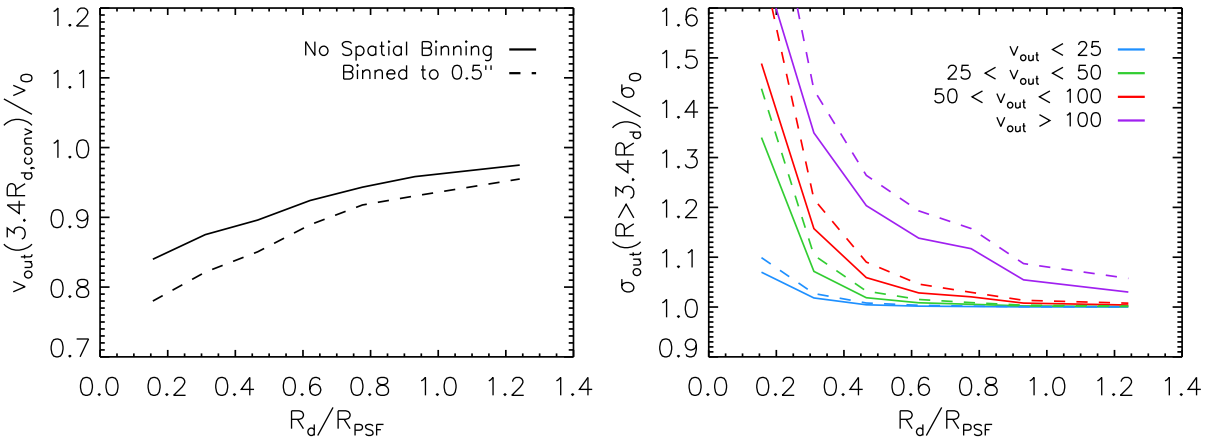

Figure B9. Effects of spatial binning on measurements of the rotation velocity and velocity dispersion. Results are generated from our mock observations when the spectrum of each pixel is fit individually (solid line) and when the signal has been binned within a 0.5×0.5 arcsec region (dashed line). In the instances where data has been binned, the rotation velocity (*left*) is underestimated by an additional ∼5–10 per cent and the dispersion (*right*) overestimated by an additional 2–3 per cent (∼5 per cent for large v_{out}).

Downloaded from https://academic.oup.com/mnras/article-abstract/474/4/5076/4655192 by University of Queensland Library user on 07 February 2020

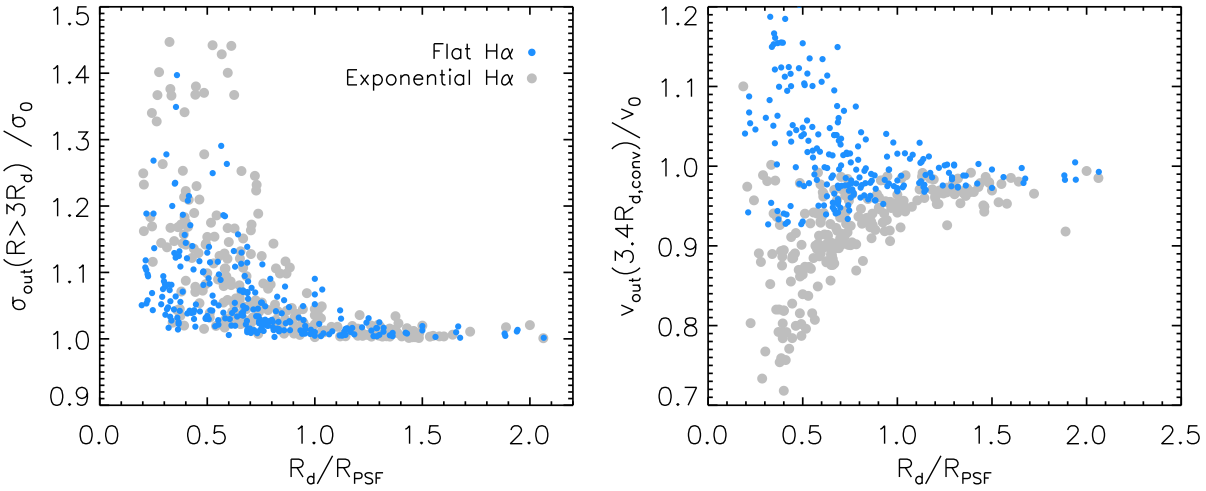

Figure B10. Beam smearing correction in v and σ as a function of the surface brightness profile. These results are generated from mock observations when the H α intensity follows an exponential profile (black points) or is uniform across the IFU (blue points). Left: For a 'flat' H α profile, effects of beam smearing on the velocity dispersion are weaker by $\sigma_{\rm out}/\sigma_0 \sim 0.1$ at low $R_{\rm d}/R_{\rm PSF}$. Right: Results for the two flux distributions diverge significantly for $R_{\rm d}/R_{\rm PSF} < 0.7$. When the H α follows a uniform distribution, the recovered rotation curve is close to the intrinsic; hence if there is a turnover within the data using the convolved radius may actually result in an overestimate of the velocity. We see that v may be overestimated by as much as 20 per cent.

[1]*Center for Extragalactic Astronomy, Department of Physics, Durham University, South Road, Durham DH1 3LE, UK*
[2]*European Southern Observatory, Karl-Schwarzschild-Str 2, D-85748 Garching b. München, Germany*
[3]*Institute for Computational Cosmology, Durham University, South Road, Durham DH1 3LE, UK*
[4]*Astrophysics, Department of Physics, University of Oxford, Keble Road, Oxford OX1 3RH, UK*
[5]*Department of Physics, Lancaster University, Lancaster LA1 4YB, UK*
[6]*Kavli Institute for the Physics and Mathematics of the Universe, 5-1-5 Kashiwanoha, Kashiwa, 277-8583, Japan*
[7]*Leiden Observatory, Leiden University, PO Box 9513, NL-2300 RA Leiden, the Netherlands*
[8]*SUPA, Institute for Astronomy, Royal Observatory of Edinburgh, Blackford Hill, Edinburgh EH9 3HJ, UK*
[9]*Department of Physics, University of Western Cape, Bellville 7535, South Africa*
[10]*Dark Cosmology Centre, Niels Bohr Institute, University of Copenhagen, Juliane Mariesvej 30, DK-2100 Copenhagen, Denmark*
[11]*Institute for Astronomy, Astrophysics, Space Applications and Remote Sensing, National Observatory of Athens, Athens, GR-15236, Greece*
[12]*Centre for Advanced Instrumentation, Durham University, South Road, Durham DH1 3LE, UK*
[13]*Sydney Institute for Astronomy, School of Physics, University of Sydney, Sydney, NSW 2006, Australia*
[14]*ICRAR, University of Western Australia Stirling Highway, Crawley, WA 6009, Australia*
[15]*ARC Centre of Excellence for All-sky Astrophysics (CAASTRO), 44-70 Rosehill Street, Redfern NSW 2016, Sydney, Australia*
[16]*Research School for Astronomy & Astrophysics, Australian National University, Canberra, ACT 2611, Australia*
[17]*Centre for Astrophysics and Supercomputing, Swinburne University of Technology, PO Box 218, Hawthorn, VIC 3122, Australia*
[18]*Australian Astronomical Observatory, 105 Delhi Rd, North Ryde, NSW 2113, Australia*
[19]*Department of Physics and Astronomy, Macquarie University, Sydney, NSW 2109, Australia*
[20]*SOFIA Operations Center, USRA, NASA Armstrong Flight Research Center, 2825 East Avenue P, Palmdale, CA 93550, USA*

This paper has been typeset from a TEX/LATEX file prepared by the author.

Downloaded from https://academic.oup.com/mnras/article-abstract/474/4/5076/4655192 by University of Queensland Library user on 07 February 2020